CrossMark

Plausible Constraints on the Range of Bulk Terrestrial Exoplanet Compositions in the Solar Neighborhood

Rob J. Spaargaren[1] , Haiyang S. Wang[2] , Stephen J. Mojzsis[3,4,5,6] , Maxim D. Ballmer[7] , and Paul J. Tackley[1]

[1] Department of Earth Sciences, Institute of Geophysics, ETH Zurich, Sonneggstrasse 5 8092, Zurich, Switzerland; rob.spaargaren@erdw.ethz.ch
[2] Institute for Particle Physics and Astrophysics, ETH Zurich, Wolfgang-Pauli-Strasse 27 8093, Zürich, Switzerland
[3] Origins Research Institute, Research Centre for Astronomy and Earth Sciences, MTA Centre of Excellence, 15–17 Konkoly Thege Miklos ut, Budapest, 1121 Hungary
[4] Department of Lithospheric Research, University of Vienna, UZA 2, Josef-Holaubek-Platz 2 A-1090, Vienna, Austria
[5] Institute for Earth Sciences, Friedrich-Schiller University, Burgweg 11 D-07749, Jena, Germany
[6] Department of Geological Sciences, University of Colorado, UCB 399, 2200 Colorado Avenue, Boulder, CO 80309, USA
[7] Department of Earth Sciences, University College London, Gower Place, London, WC1E 6BT, UK
Received 2022 August 25; revised 2022 December 7; accepted 2022 December 16; published 2023 May 5

Abstract

Rocky planet compositions regulate planetary evolution by affecting core sizes, mantle properties, and melting behaviors. Yet, quantitative treatments of this aspect of exoplanet studies remain generally underexplored. We attempt to constrain the range of potential bulk terrestrial exoplanet compositions in the solar neighborhood ($<$200 pc). We circumscribe probable rocky exoplanet compositions based on a population analysis of stellar chemical abundances from the Hypatia and GALAH catalogs. We apply a devolatilization model to simulate compositions of hypothetical, terrestrial-type exoplanets in the habitable zones around Sun-like stars, considering elements O, S, Na, Si, Mg, Fe, Ni, Ca, and Al. We further apply core–mantle differentiation by assuming constant oxygen fugacity, and model the consequent mantle mineralogy with a Gibbs energy minimization algorithm. We report statistics on several compositional parameters and propose a reference set of (21) representative planet compositions for use as end-member compositions in imminent modeling and experimental studies. We find a strong correlation between stellar Fe/Mg and metallic-core sizes, which can vary from 18 to 35 wt%. Furthermore, stellar Mg/Si gives a first-order indication of mantle mineralogy, with high-Mg/Si stars leading to weaker, ferropericlase-rich mantles, and low-Mg/Si stars leading to mechanically stronger mantles. The element Na, which modulates crustal buoyancy and mantle clinopyroxene fraction, is affected by devolatilization the most. While we find that planetary mantles mostly consist of Fe/Mg silicates, the core sizes and relative abundances of common minerals can nevertheless vary significantly among exoplanets. These differences likely lead to different evolutionary pathways among rocky exoplanets in the solar neighborhood.

Unified Astronomy Thesaurus concepts: Planetary geology (2288); Chemical abundances (224); Planetary mineralogy (2304); Galaxy chemical evolution (580)

1. Introduction

A plethora of rocky exoplanets has been documented around stars in the solar neighborhood (NASA Exoplanet Science Institute 2022). Based on formation models, it is expected that a solar-type star (i.e., an F-, G-, or K-type star) will host at least one planet (Mulders et al. 2018; Bryson et al. 2020). Thus, we can expect the catalog of discovered rocky exoplanets to grow substantially in the future. Based on first-order interpretations of mass–radius—density relationships, these "terrestrial-type" planets are inferred to share many similarities with the rocky planets in our solar system, e.g., in terms of a general, layered structure with a metallic iron core, a silicate mantle and crust, and a relatively low-mass atmosphere compared to giant planets. Those worlds not represented in our solar system, the so-called super-Earths and sub-Neptunes, are not treated here. These three fundamental layers—modulated by the physical, chemical, and mechanical properties of their constituent materials—will differ in both mass and geophysical expression(s) between planets. Consequently, rocky exoplanets may

be expected to follow different evolutionary pathways and thus sustain surface conditions that deviate, perhaps markedly, from Earth, Venus, or Mars. Owing to the fact that our current understanding of rocky planets is based on what we know from studying solar system planets, we must be prepared to challenge our assumptions of what a terrestrial-type planet is and what range of properties it could plausibly assume. As we continue to expand our methods of studying exoplanets, it makes sense to consider credible and testable physical-chemical bounds for rocky exoplanets that can help guide remote observations (Mojzsis 2022).

An important consideration that arises in terrestrial-type exoplanet studies is whether such planets are capable of supporting a mobile crust (i.e., plate-tectonics-like behavior). Alternatively, silicate and metal planets can be locked in a geodynamical regime with very little or no surface mobility (a stagnant lid), among other possibilities (e.g., a heat-pipe regime; Moore & Webb 2013; Lourenco et al. 2020). Whether a planet can sustain effective crustal recycling by processes such as plate tectonics is considered an important factor in determining its potential to host biological activity over geologic timescales (e.g., Parnell 2004; Noack & Breuer 2013; Mojzsis 2021). Evidently, the planet size affects thermal evolution and propensity toward plate tectonics (e.g., Valencia et al. 2006; O'Neill et al. 2007; Van Heck & Tackley 2011;

Stamenković et al. 2012; Stein et al. 2013). Furthermore, the interior planet structure and mantle rheology modulate thermal evolution and hence propensity toward plate tectonics (Noack & Breuer 2014; Stamenković & Seager 2016; Guerrero et al. 2018). The latter properties are modulated by bulk composition, which is a parameter that has hitherto been less studied in the exoplanetary context (Shahar et al. 2019).

While the vast majority of rocky planets are thought to consist of a metallic iron core, a rocky mantle consisting of mainly Si, Mg, and O, and a volatile atmosphere, the relative abundances of these elements will have far-reaching effects on the planet's interior properties and evolutionary pathway. The eventual size of the metallic core is a direct function of the ambient Fe abundance and oxygen fugacity of the planetary source material (Corgne et al. 2008; Rubie et al. 2015). The major-element composition of the silicate reservoir of a planet defines its mantle mineralogy, which in turn controls physical mantle parameters, such as density and viscosity (Takeda 1998; Yamazaki & Karato 2001), as well as melting behavior (Hirschmann 2000; Kiefer et al. 2015). Moreover, bulk planetary composition ultimately affects the atmospheric evolution through altering the interaction between the interior and the atmosphere (e.g., Spaargaren et al. 2020). The interior of an exoplanet can only be decoded by analysis of its atmosphere, but we need to know how interior composition affects atmospheric evolution to make sense of atmospheric observations. This work helps build the geochemical foundations for this goal, by establishing the plausible range of compositions that rocky planets can attain from analysis of stellar abundances within 200 pc of the Sun.

1.1. Star–Planet Compositional Link

A rocky exoplanet's composition cannot be directly observed, but it can be constrained by considering that the planet's composition is linked to that of its host star. A rocky planet forms from condensing material in the planet-forming disk, which consists of the same material as the forming star. Therefore, planet composition can, in principle, be estimated using the host-star composition by considering compositional fractionation during the planet formation process. Recent evidence from polluted white dwarf stars, which are stars actively accreting (exo)planetary material, demonstrates that planetary compositions indeed largely mirror stellar abundances (Doyle et al. 2019; Bonsor et al. 2021).

While the compositional link between a planet and its host star is intrinsic, it behaves differently for elements with different volatilities (Halliday & Porcelli 2001; Sossi et al. 2019; Wang et al. 2019a). Comparisons made between Earth and the Sun show that their compositions are very similar for elements with high condensation temperature in the planet-forming disk (refractory elements, such as the rare earth elements, Al and Ca; Lodders 2003), and Earth follows a depletion trend in volatile elements, i.e., elements with lower condensation temperature, such as Na, K, Rb, and Cs (e.g., Halliday & Porcelli 2001; Palme & O'Neill 2013; Wang et al. 2019a). Similar observations have also been found toward other solar system rocky bodies (particularly Mars and a variety of chondrites) relative to the Sun (Bland et al. 2005; Sossi & Fegley 2018; Yoshizaki & McDonough 2020). This solar-system-based observational phenomenon is dubbed as "devolatilization" and hypothesized to be a universal process in the formation of rocky planets (Wang et al. 2019a). In

Doyle et al. (2019), it is found that the oxidation state of extrasolar rocks inferred from the abundance measurements of polluted white dwarf atmospheres are overall consistent with that of the solar system's rocky bodies, suggesting that a similar refractory-volatile fractionation process might have also happened in the early exoplanet systems. Indeed, in Harrison et al. (2021), it is evident that post-nebular devolatilization of moderate volatiles (e.g., Na) is present in rocky exoplanetary materials that polluted white dwarfs. This offers an important piece of observational evidence for the aforementioned hypothesis.

A typical trend of devolatilization, as first quantified in Wang et al. (2019a) based on the bulk Earth and proto-Sun, reflects the observed behaviors for refractory elements and for (moderately) volatile elements as described above. The yet-limited bulk compositional data for other solar system terrestrial planets still inhabit an adequate quantitative model to be made (Lin et al. 2022), but it has been suggested in Wang et al. (2019b, 2022b) that such a trend for Mars and Venus may not be significantly different from that of Earth by taking into account the large uncertainties in their individual *bulk* compositions (e.g., Morgan & Anders 1980; Wang et al. 2018; Yoshizaki & McDonough 2020). As a first-order application for a population analysis, as aimed at here, we choose to adopt the well-quantified Sun-to-Earth devolatilization trend (Wang et al. 2019a) to take into account this important observational effect while studying rocky exoplanet bulk compositions from the measured host stellar chemical compositions (Sections 2.1 and 2.2). This will allow us to study the effects of both the intrinsic spread of the stellar chemical compositions as well as the reduced concentrations of volatile components on the geochemical and geophysical properties of rocky exoplanets, particularly those in the habitable zone around Sun-like stars. More discussion on the applicability and limitation of the approach can be found in Section 4.2.

Although stellar abundances have been proposed for constraining rocky exoplanet compositions, the foci remain on the refractory elements (e.g., Mg, Si, and Fe; Dorn et al. 2015; Unterborn et al. 2016; Dorn et al. 2017; Putirka & Rarick 2019) or on the individual planets (Wang et al. 2019b, 2022a, 2022b). Population analysis of stellar abundances—while taking into account the devolatilization effect for estimating rocky exoplanet compositions—is a gap in the literature to be filled, and is crucial for understanding further the effects of composition on planet properties. Additionally, the topic of the impact of galactic chemical evolution (GCE; Burbidge et al. 1957; Lugaro et al. 2018) on planet composition has recently joined the conversation in exoplanet science (Frank et al. 2014; O'Neill et al. 2020), but stellar compositional scatter is much larger than that predicted by GCE alone. All in all, this further warrants a population-level analysis of stellar chemical compositions and, by extension, exoplanetary compositions. Here, we apply the devolatilization trend from Wang et al. (2019a) to stellar abundance data from the Hypatia and GALAH catalogs (Hinkel et al. 2014; Buder et al. 2018) in an effort to simulate the range of bulk terrestrial exoplanet compositions. The goal is to identify in more detail what compositions need to be studied, thus providing guidance for an in-depth characterization of rocky exoplanets through future observations, experiments, as well as numerical modeling.
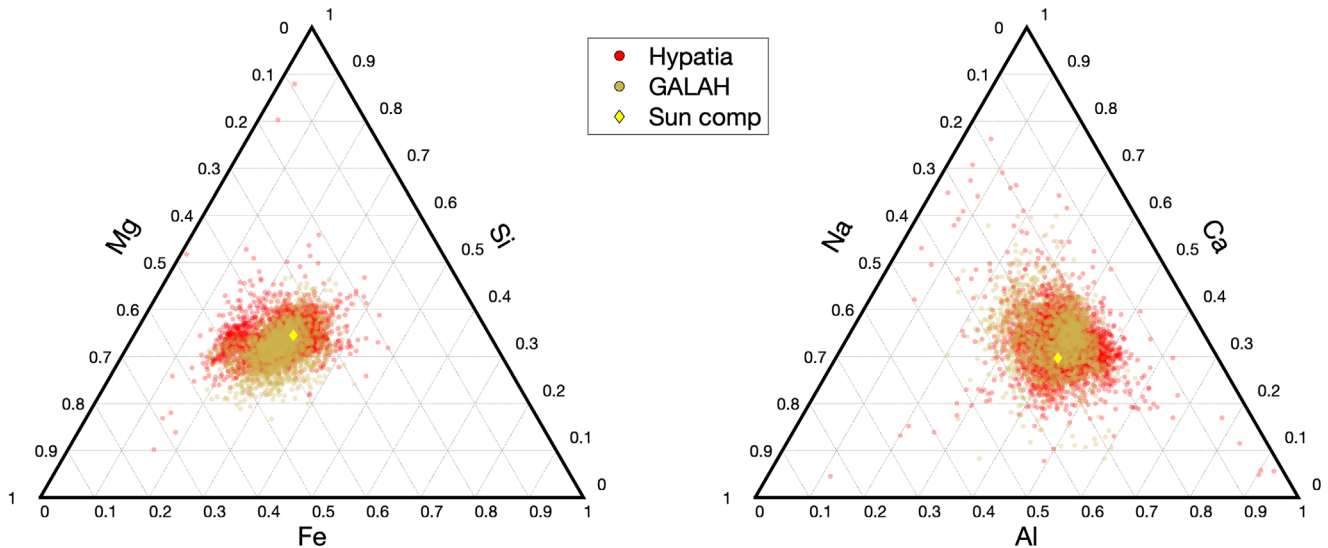
Figure 1. Stellar abundances documented in the Hypatia (red, 4236 stars) and GALAH (gold, 1971 stars) catalogs used in this study. Solar composition from Lodders et al. (2009) is plotted for comparison.

2. Data and Methodology

We explore terrestrial-type exoplanet compositions by considering rocky planets as devolatilized stars (i.e., stars that have lost most of their volatile elements). We use abundances from the Hypatia and GALAH catalogs (Section 2.1). We apply the devolatilization trend from Wang et al. (2019a; see Section 2.2) to these abundances to simulate rocky exoplanet compositions. From these compositions, core sizes and mantle compositions are estimated based on a simple model of core–mantle differentiation (Section 2.3).

2.1. Stellar Abundances

Stellar abundances from spectroscopy have been summarized in lists such as the Hypatia (Hinkel et al. 2014) and GALAH catalogs (Buder et al. 2018). Constraints from spectroscopy reflect the real stellar composition within a few per cent (Dotter et al. 2017). These observations show that stellar chemical abundances vary significantly from star to star in the solar neighborhood (Bensby et al. 2005; Valenti & Fischer 2005; Asplund et al. 2009; Lodders et al. 2009; Hinkel et al. 2014), and this chemical diversity should be reflected in the exoplanet population (e.g., Bond et al. 2010; Carter-Bond et al. 2012; Moriarty et al. 2014). We first obtained stellar abundances from the Hypatia catalog, an online (routinely updated; retrieved on 2022 July 11) database compiling measurements from a variety of literature sources (Hinkel et al. 2014). This database contains elemental abundances of >9000 stars within 500 pc from the Sun, which are all of the F, G, K, or M spectral classes. The quality and completeness of abundance data vary per star, but Fe abundances are available for all stars in the database. For converting the available data to molar abundances, and a description of error propagation throughout our work, we refer to the Supplementary Material. For some stars data from various sources are listed, which can deviate from each other by more than the reported measurement errors. In these cases, we take the median value.

Since data for stars at greater distances are sparse in this catalog, we only use abundances of those stars within 200 pc (that we here define as the solar neighborhood). Additionally, we filter for the availability of Mg and Si abundances, as these are the most abundant elements in terrestrial planets, along with Fe. Data on these elements are therefore required for assessing potential terrestrial exoplanet compositions. We also ensure that we only consider stars in the main sequence to prevent systematic errors by filtering for gravitational acceleration of those stars, $\log g > 3.5$. Finally, we exclude data for M dwarfs, which are yet to be measured accurately due to their faintness and the presence of strong molecular lines in the optical spectra (e.g., Ishikawa et al. 2020). After these filters, we proceed with abundances for 4236 stars. As previously mentioned, most Sun-like stars are expected to host planets (Mulders et al. 2018; Bryson et al. 2020), and it is still debatable if the occurrence of rocky planets depends on stellar compositions (Melendez et al. 2009; Buchhave et al. 2012; Liu et al. 2020); as such, we do not filter this data for confirmed exoplanet hosts.

Some concerns have been raised regarding systematic errors in the Hypatia catalog since its data originate from a variety of literature sources with different methodologies, as discussed in Hinkel et al. (2016). To test the robustness of using this catalog, we consider another inventory of stellar abundances that is intrinsically based on measurements with the same instruments, methodology, and data-processing methods. The GALAH catalog (Buder et al. 2018) fits these criteria and is regarded as a reliable data source of stellar abundances. It is also an independent data set, as it shares only five stars with the Hypatia catalog (Clark et al. 2021). Target selection for the GALAH survey was based on the Two Micron All Sky Survey catalog (De Silva et al. 2015), which had no available abundance measurements for Hypatia to include. We compare the data of the two catalogs after applying the same filters described above. Since the GALAH database does not focus on the solar neighborhood—the majority of its stars lie further than 200 pc—our filters (including the distance filter) leave just 1971 stars for this catalog. A comparison of the two catalogs shows that the Hypatia data display a somewhat wider range of compositions, but this may be in part due to the larger number of stars considered (Figure 1). The spread caused by systematic errors in the Hypatia catalog seems to be within the bounds of our population spread. Since we find no systematic differences in the data sets of both catalogs (within 200 pc), we merge both data sets and continue with the compositions of 6207 stars.

2.2. From Stellar to Planetary Abundances

We begin with the assumption that stellar abundance data forecast bulk terrestrial exoplanet compositions by presupposing that the observed stellar abundances are a good representation of the planet-forming disk composition. This premise has its basis in the fact that >99% of the mass of any individual star–planet system is that of the star. Further, we assume that terrestrial planet composition is equivalent to the host-star composition after applying depletion factors based on the devolatilization trend. This assertion has merit as CI chondritic elemental abundances are a good match for devolatilized solar abundances (for both refractories and moderate volatiles; Anders & Grevesse 1989) and for bulk-Earth compositions (for refractories only; Wang et al. 2019a). We model bulk terrestrial exoplanet compositions based on the Sun-to-Earth devolatilization factors (Table 1) from Wang et al. (2019a). We consider key rock-forming elements based on their volatility as represented by the 50% condensation temperature, T_c, from Lodders (2003). We choose to use condensation temperatures from Lodders (2003) as these are the most widely used in the literature, and our analysis has shown that other estimates (e.g., Wood et al. 2019) do not deviate significantly for the elements considered herein. We apply these correction factors (Table 1) directly to the stellar abundances and normalize them to yield bulk-planet molar fractions. This application also implicitly confines the planets we consider to the habitable zones around these Sun-like stars. We discuss the applicability and limitations of this devolatilization process in more detail in Section 4.2.

In this work, the elements under consideration are O, Fe, Mg, Si, Ca, Al, Na, S, and Ni; these elements are the most abundant and/or the most critical in terms of their roles in interior properties. The most abundant elements in solar system terrestrial planets are Fe, Mg, and Si (Wänke & Dreibus 1994; McDonough & Sun 1995), and these are also found to be the most abundant refractory elements in all stars in our sample. Additionally, Fe directly affects core size, whereas mantle viscosity depends on the relative abundances of Mg and Si (see below). We include oxygen because of its role in determining core size and forming oxides and silicates. Of the elements not relatively depleted in planets due to their high condensation temperatures, Ca and Al are by far the most abundant, and we therefore consider them. Both elements are likewise important because they influence the interior properties, as Ca affects lower-mantle mineralogy by stabilizing Ca-perovskite, while Al can affect melting behavior and water storage capacity in minerals. Na, while less abundant, significantly affects melting behavior and crustal buoyancy (Unterborn et al. 2017). Finally, Ni and S affect core size and density, and are therefore also considered.

2.3. Core–Mantle Differentiation

We separate the modeled bulk planetary compositions into silicate-mantle and metallic-core chemical reservoirs. The size of the core reservoir, and the distribution of Fe between the core and mantle, depends on the amount of oxygen available for oxidation of cations up to iron. However, oxygen availability, expressed as oxygen fugacity (fO_2), is unfortunately not predictable based on stellar abundances. Oxygen has a dual nature during planet formation as both a volatile (in compounds such as H_2O and CO) and as a refractory (in

Table 1
Depletion Factors of All Elements

Element	T_c (K)	Depletion Factor
O	875[a]	0.810 ± 0.011
Na	958	0.738 ± 0.013
Mg	1336	0.148 ± 0.047
Al	1653	0
Si	1310	0.205 ± 0.043
S	664	0.929 ± 0.007
Ca	1517	0
Fe	1334	0.155 ± 0.047
Ni	1353	0.109 ± 0.051

Notes. Based on the devolatilization trend from Wang et al. (2019a), alongside condensation temperatures from Lodders (2003), on which the depletion factors are based.
[a] The condensation temperature of oxygen was modified by Wang et al. (2019a) by considering the nature of oxygen being both a volatile and refractory element.

silicates, which are all oxides) element, and its 50% condensation temperature therefore depends nonlinearly on stellar composition (see, e.g., Unterborn & Panero 2017 for the effects of Mg and Si). Further, accretion of volatile species increases the bulk-planet oxygen fugacity and therefore reduces core size, but accretion of these compounds is not well understood even for the solar system planets (see, e.g., Rubie et al. 2015; O'Neill 2020). Therefore, we make some assumptions to estimate the amount of oxygen available during core formation.

Recent studies of polluted white dwarfs show remarkably uniform estimated oxygen fugacities in terrestrial exoplanets (Doyle et al. 2019). This observation leads to the expectation that planets with a similar formation history as Earth would have a similar oxygen fugacity. We therefore model core–mantle differentiation by assuming a fixed Earth-like bulk molar Fe/FeO ratio, and therefore fixed fO_2 (see Section 4.3 for a continued discussion). Accordingly, the core size purely depends on the bulk-planet Fe abundance, similar to the approach used in O'Neill et al. (2020). Below, we will mostly consider cases with an Earth-like molar Fe/FeO of 6.31 (McDonough 2003; Wang et al. 2018), but we also consider some cases with variable fO_2 (to be detailed in Section 3.3).

In contrast to Fe, all Ni and S is assumed to be partitioned into the core due to their high reducing potential and siderophile behavior (McDonough 2003). We further assume that the core contains 5 wt% Si (Shahar et al. 2009; Javoy et al. 2010; Ziegler et al. 2010; Hirose et al. 2013) and 2.5 wt% O (McDonough 2003; Javoy et al. 2010; Hirose et al. 2013) as additional light elements, independent of core size and core formation conditions. The light-element budget of the core depends on the planet formation scenario and planet size (Wade & Wood 2005), among other factors, but we only consider planets with one Earth radius, and the resulting differences would not be significant compared to observational errors.

3. Results

We estimate bulk rocky exoplanet compositions in the solar neighborhood by applying depletion factors based on the devolatilization trends from Wang et al. (2019a) to stellar abundance data in the solar neighborhood (Hinkel et al. 2014; Buder et al. 2018). We find that the differences between stellar and planetary compositions are small for the primary rock-
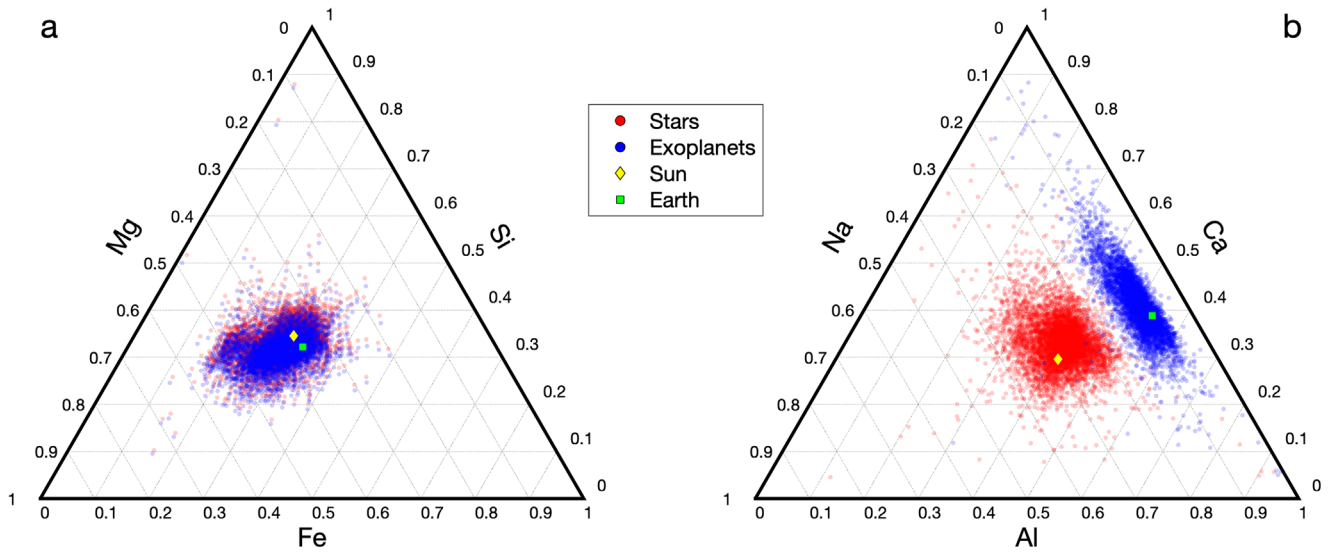
Figure 2. Bulk compositions of stars in the solar neighborhood (red; Hinkel et al. 2014; Buder et al. 2018), planet compositions calculated in this work (blue), solar composition (yellow diamond; Lodders et al. 2009), and Earth composition (green square; McDonough 2003) molar compositions, in the Fe–Mg–Si (left) and Ca–Al–Na (right) systems.
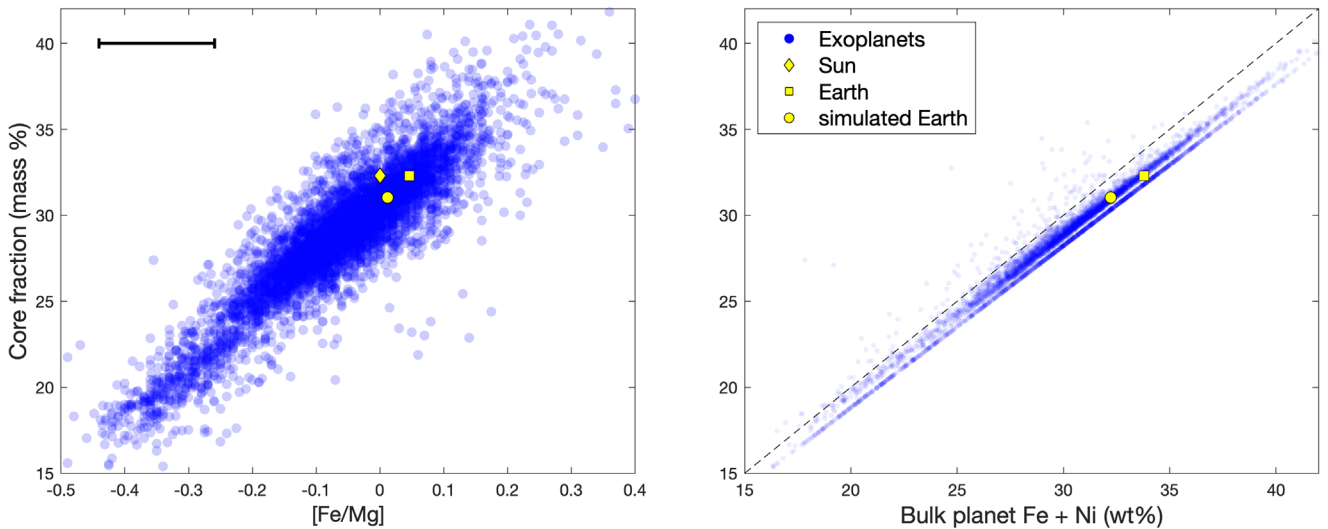

Figure 3. Core sizes of terrestrial-type exoplanets (mass fraction) as a function of stellar [Fe/Ni] (in dex, left), and of bulk-planet Fe+Ni abundance (wt%, right). An indication of the typical measurement error on [Fe/Mg] is shown. Core sizes are based on an iron distribution between core and mantle according to an Earth-like Fe/FeO, and cores containing all nickel and sulfur present in the planet, plus 2.5 wt% O and 5 wt% Si. Earth has a core size of 32.3 wt% for a bulk Fe+Ni content of 33.8 wt% (McDonough 2003). The dashed line represents the trend for pure Fe-Ni cores where all Fe and Ni is present in the core. The "simulated Earth" value is retrieved by applying our methodology to the protosolar composition from Wang et al. (2019a). The solar value shown is from Lodders et al. (2009). The GALAH catalog does not report S abundances, therefore a part of our population has noticably smaller cores due to the absence of S.

forming cations (i.e., major elements on Earth) such as Fe, Mg, and Si (Figure 2(a)), since these elements have similar condensation temperatures in the planet-forming disk. Planets are slightly depleted in Si and Fe relative to more refractory elements (e.g., Ca and Al). In detail, they are more depleted in Si than in Fe, but not by very much. The depletion of terrestrial planets is more pronounced for moderately volatile elements such as Na (Figure 2(b)), the effect of which is shown and discussed later (Sections 3.4 and 4.2). In contrast, the highly refractory elements Ca and Al are not depleted in terrestrial planets compared to their host stars.

3.1. Core Sizes

To understand long-term planetary evolution and interior-exterior coupling, it is important to constrain mantle compositions based on bulk-planet composition. Core–mantle differentiation is highly efficient for most elements, which are effectively partitioned into either the core or mantle. In contrast, Fe can enter both the mantle (as iron oxides and in silicates) and core (as Fe^0), controlled by the availability of oxygen (i.e., the oxygen fugacity). We assume that iron partitions between the core and mantle in a similar way as on Earth (i.e., Fe/FeO is equal to that of Earth; see Section 2.3). This assumption leads to a nearly linear trend of core size with bulk-planet Fe abundance (Figure 3). Further, bulk-planet Fe abundance is a function of stellar [Fe/Mg], and therefore a simple linear trend exists between stellar [Fe/Mg] and core mass. Deviation from linearity in either trend stems from light elements in the core, as we assume that all S is partitioned into the core. Based on our model, Earth's core size is close to the

population average. While our simulated Earth composition (based on the protosolar composition from Wang et al. 2019a) can deviate from the composition presented by McDonough (2003; see Figure 3), there are multiple estimates in the literature that deviate from theirs (e.g., Wang et al. 2018). Further, the measurement errors on stellar abundances are typically large enough to allow for these deviations.

Variation in stellar S content leads to a diversity in core light-element fraction among rocky exoplanets, under our assumption that all S is partitioned into the core. All exoplanets in our population have core light-element fractions of at least 7.5 wt%, as we assume that rocky planet cores contain 5 wt% Si and 2.5 wt% O, similar to the Earth's core. Further addition of S increases the light-element fraction to between 8 and 12 wt%. (Figure A7(a)). There seems to be a minor trend where the core S fraction is slightly higher for smaller cores (Figure A7(b)), so small cores are also slightly less dense than large cores. Further, the core Ni content can vary from 5 to 9 mol% (cf. 6% in Earth), having a limited effect on core sizes (Figure A7(d)).

3.2. Mantle Compositions

We estimate rocky exoplanet mantle compositions by subtracting the simulated core size and composition from the bulk compositions. The most abundant cations in the Earth's mantle are Fe, Mg, and Si, dubbed major elements. The other elements (aside from O, Ca, Al, Na, S, and Ni) are referred to as minor elements below. The abundances of Mg and Si are often conveyed as the Mg/Si ratio, as this is an indicator for the relative abundances of common mantle minerals, such as olivine ($(Mg,Fe)_2SiO_4$) and pyroxene ($(Mg,Fe)SiO_3$) in the upper mantle, or bridgmanite ($(Mg,Fe)SiO_3$) and ferropericlase ($(Mg,Fe)O$) in the lower mantle. Further, it indicates the appearances of minerals which are rare on Earth, such as ferropericlase in the upper mantle at high Mg/Si, or quartz at low Mg/Si (see Sections 3.4 and 4.4). Most planets we consider here have mantle Mg/Si ratios between 0.8 and 2.2 (see Figure 4(a)). The bulk silicate Earth with a Mg/Si ratio of 1.2 may therefore be viewed as below average. Notable is that planet mantle Mg/Si is typically 15%–20% higher than stellar Mg/Si, with about a 7% increase due to the difference in depletion factors (see Table 1), and a further depletion due to the presence of Si in the core.

The planets in our population also have mantle iron contents of 3–7 wt% (Figure 4(b)). The Earth is above average in terms of mantle iron content, at 6.26 wt%. This is also reflected in the mantle Mg# (molar Mg/(Mg+Fe)), where the Earth (0.89) is accordingly below average (0.87–0.95; Figure 4(d)).

The abundance of minor elements is an indicator of how exotic an exoplanet composition is. The minor elements, Ca, Al, and Na, are significantly less abundant than Mg, Fe, and Si in the solar system planets. Here, we define the minor-element fraction as $X_{minor} = (Ca + Al + Na)/(Ca + Al + Na + Fe + Mg + Si)$. In our terrestrial-type exoplanet population, X_{minor} ranges from 6 to 13 molar per cent (see Figure 4(c)). Therefore, we find that exotic compositions with extreme abundances of minor elements are rare, consistent with inferences from GCE (Alibés et al. 2001). Relative abundances of minor elements vary, as illustrated by the molar Ca/Al ratios, which show a significant skew (i.e., tail at high Ca/Al; see Figure 4(e)). The Na mantle abundance shows a similar shape to the Ca/Al distribution and is consistently low for all exoplanet

compositions (Figure 4(f)). From our analysis, we can conclude that Earth is close to the median value in terms of total minor-element abundance, Ca/Al ratio, and Na abundance.

3.3. Representative Compositions

Next, we select 21 representative compositions for our population of modeled rocky exoplanets. These compositions are chosen such that they span the compositional range inferred by our approach, and also capture key trends in the data set. We study these representative compositions further by simulating the mantle mineralogy of each of these model planets. These representative compositions may be used as a convenient reference data set for further studying the effects of rocky exoplanet composition.

The terrestrial-type exoplanet mantle compositions we retrieve can be described to first order by normal distributions (Figure 4). Table 2 provides the average value and 2σ range of key compositional properties. However, the data set also displays systematic compositional trends that are not captured by simple normal distributions (Figure 5), likely due to chemical trends in the galaxy (e.g., Bensby et al. 2011). For example, planets with high core mass tend to have lower Mg/Si (see Figure 5(a)), as stellar Mg/Si tends to decrease with increasing iron abundance due to GCE (see Section 4.1). For a full overview of all compositional trends, please refer to Figure A8.

Because of the presence of compositional trends, we define a number of representative compositions that capture these trends to study in more detail, rather than studying planet compositions at the 2σ limits. Our 21 representative compositions represent the full compositional range (within 95% confidence levels) of the distribution of our modeled exoplanets (Table 2). We arrive at these 21 representative planet compositions by combining three approaches. First, we pick eight actual samples from our (devolatilized) data set. These *sample-based* compositions are chosen so as to span the compositional range for all parameters. Next, we define nine *synthetic* planet compositions based on the 2σ limits of our exoplanet distribution in terms of mantle Mg/Si, core size, and bulk-planet Fe+Mg+Si, to study the effects of varying Fe, Mg, and Si individually, as these are the most abundant cations in all exoplanets. Finally, we define four additional synthetic planet compositions, dubbed synthetic-fO_2, with different bulk fO_2 and therefore different Fe/FeO, to test our assumption of Earth-like Fe/FeO. The mantle compositions and core sizes of these 21 representative compositions can be found in Table 3.

3.3.1. Sample-based Compositions

To begin with, eight sample-based compositions are selected from our simulated planet population, earmarked by applying the selection criteria below until only a few planets remain, at which point the best sample is selected by hand. We summarize these selection criteria both in the text and in Table 4. These sample-based compositions are divided into high-Fe/Mg and low-Fe/Mg planets, and we define four compositions for each of these subsets. Planets with high Fe/Mg exhibit the highest core masses and lowest Mg/Si ratios. Thus, we select one composition with high core mass fraction (CMF) and relatively high Mg/Si ("sample high M_c"), and one composition with low Mg/Si and relatively low CMF ("sample low Mg/Si"). High CMFs are typically associated with low Na abundances (Figure 5(c)), as well as average Ca/Al and minor-element
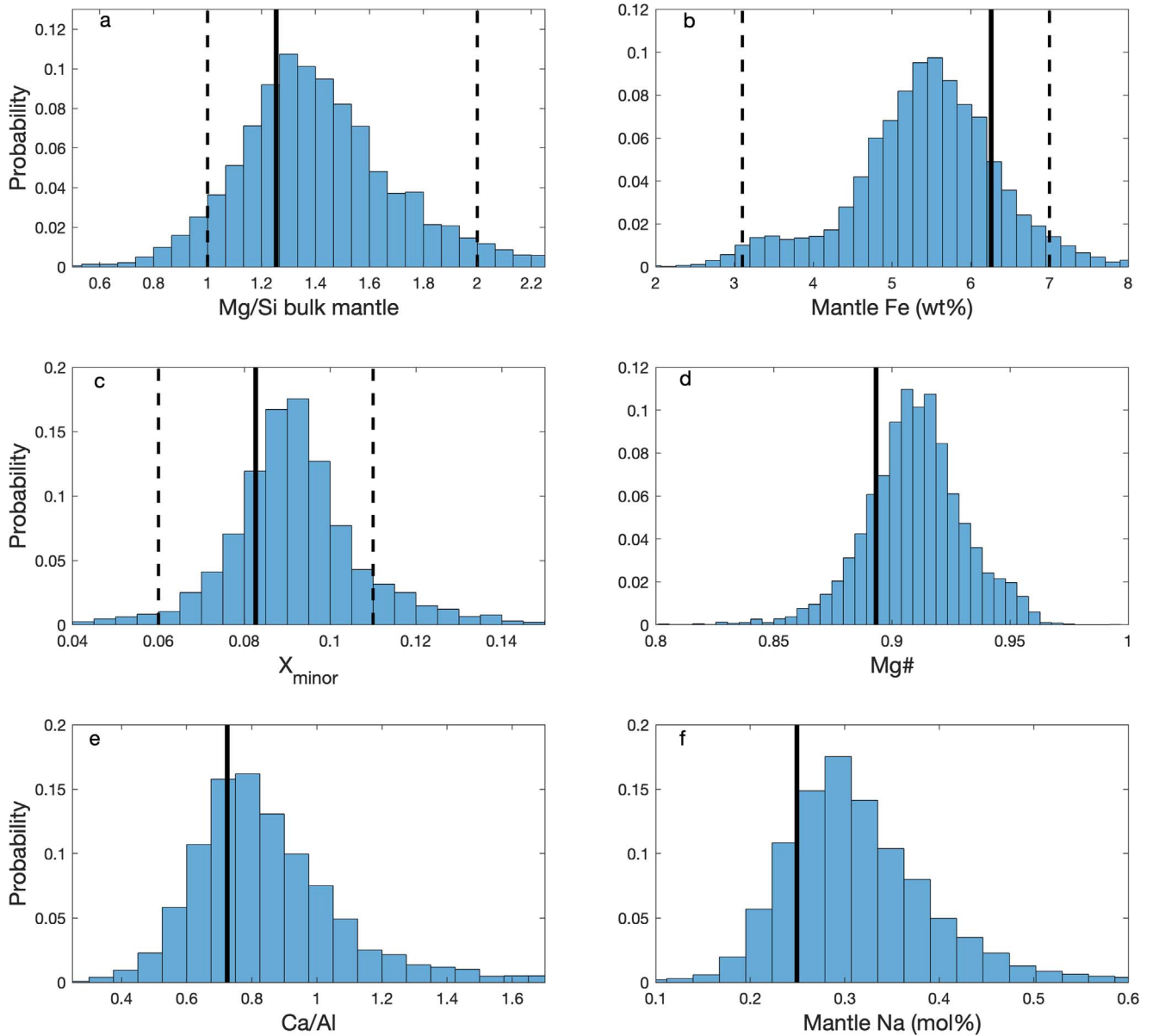
Figure 4. Histogram of terrestrial-type exoplanet mantle compositions, in terms of molar Mg/Si ratios (a), iron abundance in wt% (b), molar fraction of minor elements (i.e., Ca, Al, and Na; (c)), molar Mg number (MgO/(MgO+FeO); (d)), molar Ca/Al ratios (e), and mantle molar Na abundance (f). For comparison, the Earth's composition is plotted as a solid black line (Mg/Si = 1.25, 6.26 wt% Fe, 8.21% minor elements, Mg# = 0.89, Ca/Al = 0.73, 0.25 mol% Na; McDonough 2003). The synthetic representative compositions (Section 3.3) are shown in panels (a), (b), and (c) as dashed lines.

fractions (Figure A8), so "sample high M_c" represents these trends. Low Mg/Si is typically associated with low minor-element fractions and average Na abundances (Figure A8): "sample low Mg/Si" is chosen to reflect these characteristics. We further take a composition with high Ca/Al ratios ("sample high Ca/Al") and another one with high minor-element abundances ("sample high minor"), as these characteristics are typically related to high-Fe/Mg compositions (Figure 5(b) and Figure A8). The former is associated with lower-than-average minor-element fractions (Figure 5(d)). The latter is associated with low Ca/Al (Figure 5(d)) and average Mg/Si (Figure 5(b)).

Planets with low Fe/Mg exhibit the lowest core masses and highest Mg/Si ratios. To reflect these systematics, two planets are chosen based on low core mass ("sample low M_c") and high Mg/Si ("sample high Mg/Si"), respectively. The former is

associated with the lowest Na abundances (Figure 5(c)), and average Ca/Al and minor elements (Figure A8). The latter is associated with below-average Ca/Al ratios (Figure 5(b)), but average minor-element fractions and Na abundances (Figure A8). Further, we include a planet with high Na abundances among the low-Fe/Mg cases ("sample high Na"), which corresponds to a high CMF for the low-Fe/Mg planets (Figure 5(b)), as well as fairly high Ca/Al. Finally, we choose a composition with very low minor-element fractions ("sample low minor"), which corresponds to low Mg/Si ratios (Figure A8).

3.3.2. Synthetic Compositions

Next, eight of the nine *synthetic* compositions are based solely on varying core size, mantle Mg/Si, and mantle minor-element fractions. These quantities together span the bulk-planet Fe, Mg, and Si fractions and have the most significant
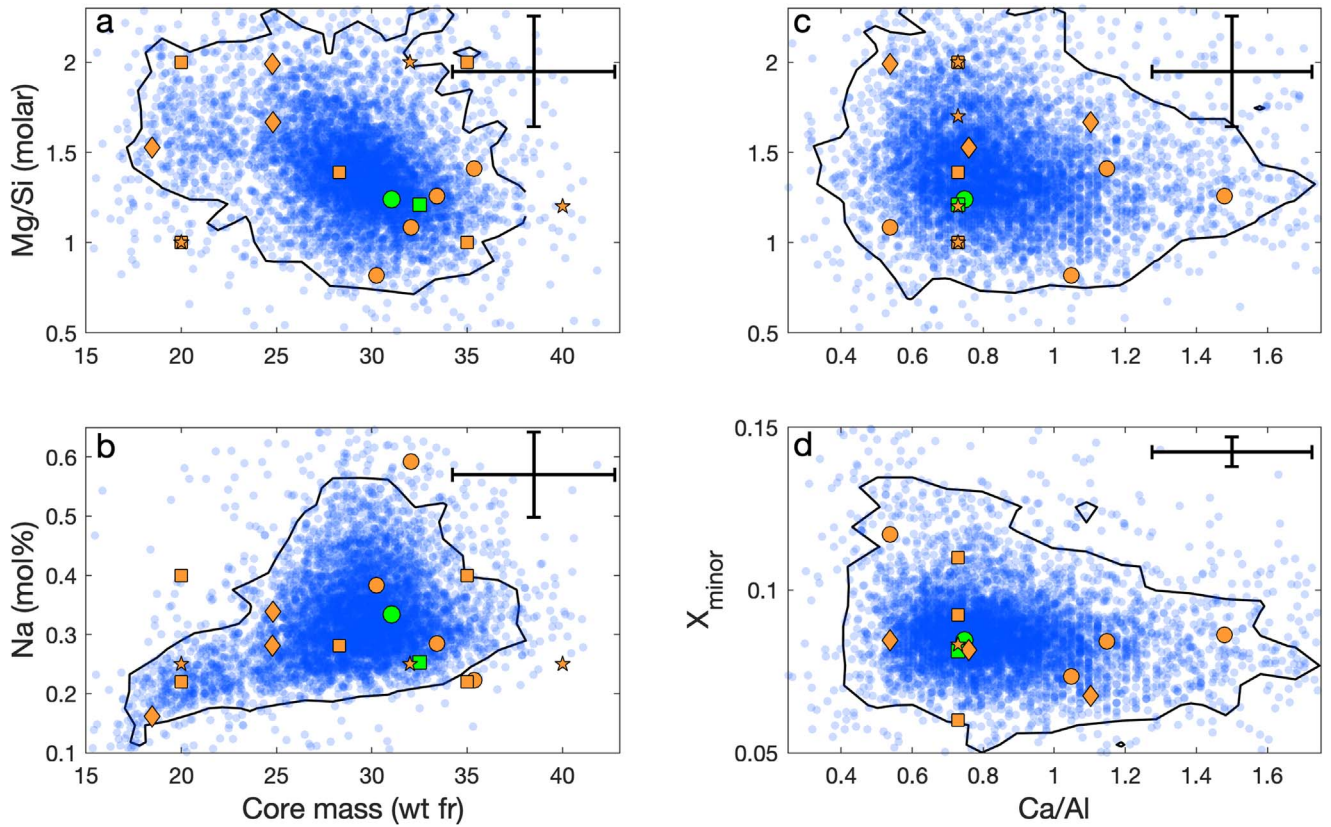
Figure 5. Scatter plots of bulk terrestrial exoplanet compositions for a few chosen compositional quantities, showing compositional trends. The contours contain 95% of the modeled compositions. Orange dots and diamonds show the high-Fe/Mg and low-Fe/Mg *sample-based* compositions, respectively, the orange squares show the eight *synthetic* compositions, and the orange stars show the four synthetic-fO_2 compositions. Note that composition synthetic-fO_2 4 falls outside the range plotted in panels (a) and (c) (see Figure A8). The light green square represents the Earth's composition (McDonough 2003), while the light green circle represents the composition of a simulated planet based on a star with a protosolar composition (Wang et al. 2019a). Error bars are based on combined uncertainties of stellar abundance measurements from the Hypatia and GALAH catalogs (Hinkel et al. 2014; Buder et al. 2018) and of the devolatilization trend (see Table 1).

Table 2
Statistics of Terrestrial-type Exoplanet Compositions in the Solar Neighborhood

Parameter	Median	2σ Range	Earth
Mg/Si	1.39	(0.78, 2.18)	1.25
Mantle Fe (wt%)	5.48	(3.17, 7.57)	6.26
Mg#	0.91	(0.86, 0.95)	0.89
X_{minor}	9.24	(4.99, 13.66)	8.21
Ca/Al	0.88	(0.45, 1.62)	0.73
Na	0.321	(0.183, 0.549)	0.25
Core mass (wt%)	28.48	(18.94, 35.57)	32.3
Core S	4.25	(1.99, 10.96)	1.9

Note. Mantle (top half) and core (bottom half) compositions are in mol% (or molar ratios) unless specified otherwise. Values for Earth from McDonough (2003) are given for comparison. Mg# is defined as molar mantle Mg/(Mg+Fe).

effect on the interior properties. For other elements, their fractions in the *synthetic* compositional cases are assumed to be equal to Earth's, allowing us to study the effects of varying Fe, Mg, and Si alone. We use mantle molar Mg/Si, with upper and lower bounds of 1.0 and 2.0 (Figure 4). Further, we use CMFs of 20 and 35 wt%. This also defines mantle Fe fraction, as we assume an Earth-like core S content and that fO_2 is constant, to be between 1.3 and 2.8 mol% (corresponding to mantle FeO weight percentages of about 3.1–7.0). Finally, we define the

synthetic compositions using mantle minor-element fractions of 6 and 11 mol%, as this also determines the bulk mantle Fe+Mg +Si content. We include a ninth *synthetic* composition based on the median values of core size, mantle Mg/Si, and minor-element fraction (see Table 2). Figure A8 shows that the nine synthetic and the eight sample-based compositions cover the full range of inferred rocky exoplanet compositions.

3.3.3. fO2-based Compositions

While these 17 compositions are selected based on the assumption of Earth-like fO_2 during core formation, we also consider four cases with variable fO_2 for comparison. To constrain these four compositions, we recalculate core–mantle differentiation for all of our hypothetical 6207 planets based on observed stellar oxygen-to-refractory-element ratios (as opposed to the assumption of a fixed Fe/FeO as above). Applying the Earth–Sun oxygen devolatilization factor results in planets with oxygen-to-cation ratios between 0.5 and 2.06, where 1.0 means sufficient oxygen is available to oxidize all cations to oxides, including all metallic iron. However, we expect that coreless exoplanets are rare, as planetary material accreting onto polluted white dwarf stars typically comes from planets that differentiated into a mantle and core (e.g., Hollands et al. 2018; Doyle et al. 2019; Bonsor et al. 2020). Further, we consider that planets with elements other than Fe and Ni that are reduced to a metallic state due to exceptionally low oxygen budget are also rare. Therefore, we assume that the oxygen

Table 3
Core Sizes and Mantle Oxide Compositions of the 21 Representative Compositions[a]

Composition	M_c	Na_2O	MgO	Al_2O_3	SiO_2	CaO	FeO
Earth	32.5	0.30	48.24	2.23	39.85	3.25	5.96
Sample high M_c	35.1	0.27	50.48	1.87	35.76	4.29	6.90
Sample low Mg/Si	30.1	0.42	40.11	1.59	48.92	3.33	5.46
Sample high minor	31.4	0.75	44.66	3.48	41.17	3.74	6.12
Sample high Ca/Al	33.3	0.35	48.29	1.63	38.40	4.82	6.42
Sample low M_c	18.2	0.20	55.03	2.26	36.06	3.43	2.78
Sample high Mg/Si	24.4	0.33	59.86	2.60	30.08	2.80	3.90
Sample high Na	24.6	0.40	56.77	1.44	34.06	3.17	3.92
Sample low minor	20.3	0.26	49.49	1.30	42.79	2.78	3.38
Synthetic 1	35	0.42	56.91	2.98	28.45	4.34	6.67
Synthetic 2	35	0.22	59.43	1.60	29.73	2.33	6.58
Synthetic 3	35	0.42	42.49	2.98	42.49	4.34	7.06
Synthetic 4	35	0.22	44.36	1.60	44.36	2.35	6.99
Synthetic 5	20	0.42	59.26	2.98	29.63	4.36	3.11
Synthetic 6	20	0.22	61.76	1.61	30.88	2.34	3.07
Synthetic 7	20	0.42	44.36	2.99	44.36	4.34	3.30
Synthetic 8	20	0.23	46.22	1.60	46.22	2.34	3.27
Synthetic 9	28.3	0.34	51.0	3.37	36.66	3.69	4.99
Synthetic-fO_2 1	40	0.31	50.60	2.23	42.17	3.27	1.25
Synthetic-fO_2 2	32	0.31	61.89	2.24	30.93	3.27	0.24
Synthetic-fO_2 3	20	0.32	38.40	2.24	38.40	3.27	17.20
Synthetic-fO_2 4	7	0.32	50.24	2.24	29.56	3.27	14.21

Note.
[a] Core size is in weight percent, mantle oxide composition is in molar percent.

Table 4
Compositional Trends from which the Eight Sample-based Representative Compositions Have Been Chosen

Defining Characteristic	Fe/Mg	Typical M_c	Typical Mg/Si	Typical Minor Fraction	Typical Ca/Al	Typical Na
Sample high M_c	High	Very high	Average	Average	Average	Low
Sample low Mg/Si	High	Average	Very low	Low	Average	Average
Sample high minor	High	Average	Average	Very high	Low	Very high
Sample high Ca/Al	High	High	Average	Low	Very high	Average
Sample low M_c	Low	Very low	High	Average	Average	Very low
Sample high Mg/Si	Low	Low	Very high	Average	Low	Average
Sample high Na	Low	Low	High	Low	High	High
Sample low minor	Low	Low	Low	Low	Average	Low

Note. Trends are defined based on Figure 5 and Figure A8.

depletion factor scales with stellar oxygen-to-refractory-element ratios in such a way that both coreless and extremely reduced (with other cations than Fe and Ni in the core) fall on the edges of the 95% confidence level, and so the distribution accurately reproduces the Earth–Sun oxygen depletion factor (Table 1). We choose the four compositions near the edges of the 95% confidence level of the remaining planetary oxygen budget distribution (Figure A6), as well as upper and lower bulk-planet Mg/Fe values. This approach results in planet Fe/FeO values between 0.16 and 56.4.

3.4. Mantle Mineralogy

Finally, we model mantle mineralogical profiles for each of these 21 representative planet compositions. To this end, we employ a Gibbs free energy minimization algorithm, Perple_X (Connolly 2005), using the thermodynamic database from Stixrude & Lithgow-Bertelloni (2022). This algorithm estimates the stable mantle mineralogy as a function of pressure and temperature. We simulate mantle mineralogy based on the present-day Earth mantle adiabat (Brown & Shankland 1981), up to the core–mantle boundary pressure of any given planet, which depends on core size and bulk iron abundance (according to Equation (16) from Noack & Lasbleis 2020). Generally, the mineralogical profiles of the representative cases are similar to those of Earth, with the upper mantle mainly consisting of olivine (and its high-pressure polymorphs wadsleyite and ringwoodite; $(Mg,Fe)_2SiO_4$), pyroxene $((Mg,Fe)SiO_3)$, and garnet $((Ca,Mg,Fe)_3(Al,Fe)_2Si_3O_{12})$, and the lower mantle consisting of bridgmanite and post-perovskite $((Mg,Fe)SiO_3)$, ferropericlase $((Mg,Fe)O)$, and Ca-perovskite $(CaSiO_3)$. However, the relative abundances of these minerals vary significantly among these planets (Figure 6).
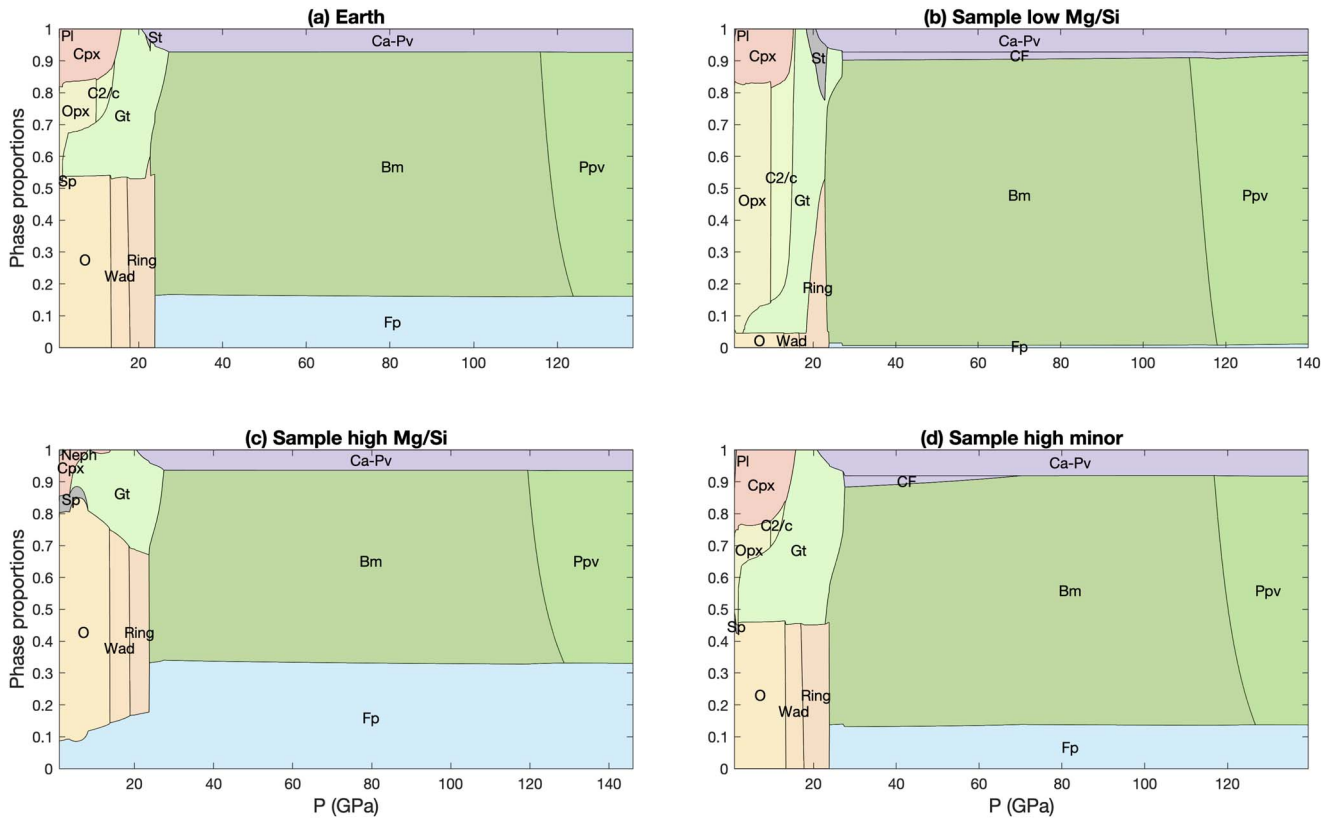
Figure 6. Mineralogical profiles of Earth (composition from McDonough 2003) and three selected representative compositions (see Table 3), showing mineralogical diversity. Pressure is shown from the surface (left side of each profile) to the core–mantle boundary pressure (right side), determined from Equation (16) of Noack & Lasbleis (2020). Mineralogical assemblages are calculated with Perple_X (Connolly 2005), using the thermodynamic database from Stixrude & Lithgow-Bertelloni (2022). O: olivine, Opx: orthopyroxene, Cpx: clinopyroxene, C2/c: C2/c pyroxene, Neph: nephline, Q: quartz, Pl: plagioclase, Sp: spinel, Gt: garnet, Wad: wadsleyite, Ring: ringwoodite, St: stishovite, Bm: bridgmanite, Fp: ferropericlase, Ca-Pv: Ca-perovskite, CF: Ca-ferrite, Ppv: post-perovskite.

In detail, Earth is dominated by olivine and bridgmanite, with pyroxene, garnet, and ferropericlase as the main secondary phases (Figure 6(a)). In planets with low Mg/Si (Figure 6(b)), the olivine fraction is significantly lower, and the upper mantle consists primarily of pyroxene and garnet. Further, ferropericlase abundances in the lower mantle of these planets approach zero. In turn, planets with high Mg/Si contain significantly more olivine and ferropericlase in their mantles (Figure 6(c)). Further, the most Mg-enriched planets contain ferropericlase in the upper mantle, even at very low pressures. Planets with sufficiently high Mg/Si to contain ferropericlase in the upper mantle also completely lack orthopyroxene, while clinopyroxene and garnet are still present to accommodate Na, Al, and Ca. Finally, planets with high minor-element abundances have higher abundances of minerals such as Ca-perovskite, Ca-ferrite, and clinopyroxene (Figure 6(d)). However, even in these planets the primary phases remain the Fe, Mg silicates olivine, pyroxene, bridgmanite, and ferropericlase.

As seen in the mineralogical profiles of our representative compositions, Mg/Si is an important control on the main mantle mineralogy. Assuming an otherwise Earth-like composition shows important transitions in upper-mantle mineralogy, where for Mg/Si $\geqslant$ 1.6 ferropericlase becomes present, while for Mg/Si $\leqslant$ 0.8 the SiO$_2$ minerals quartz and stishovite appear (Figure 7). Note that quartz-bearing mantles fall just outside of our compositional spread (Figure 4(a)). Further, a transition from olivine dominated to pyroxene+garnet dominated occurs around Mg/Si = 1.1. High Mg/Si also tends to stabilize spinel

in the upper mantle. In the lower mantle, the ferropericlase abundance increases almost linearly with Mg/Si for Mg/Si $\geqslant$ 0.8, where stishovite is not present. These transitions may differ somewhat with varying Ca, Al, and Na abundances, but are fairly robust (Figure A9).

Both Ca and Na tend to stabilize the mineral clinopyroxene, where Ca stabilizes it at the cost of garnet, while Na stabilizes it at the cost of orthopyroxene (Figure 8). This trend is observed for a wide range of compositions within our population (Figure A10). Olivine is also further stabilized by increasing Na, and to some extent by increasing Ca, as more Si is used to form clinopyroxene rather than garnet or orthopyroxene. Meanwhile, Ca only has a small effect on the Ca-perovskite abundance for the compositional range we find here (Figure 4(e)). Both Ca/Al and Na do not significantly affect lower-mantle mineralogy.

4. Discussion

4.1. Stellar Parameters

Based on stellar abundances and models for devolatilization and core–mantle partitioning, we constrain the compositional range of rocky exoplanets in the solar neighborhood. Due to the limited range of stellar Fe abundances, we find that rocky exoplanets have cores that are usually less massive than their mantles. Further, as stars tend to be rich in Fe, Mg, and Si compared to other refractory elements, we find that the minor-element abundances are consistently low (Table 2),
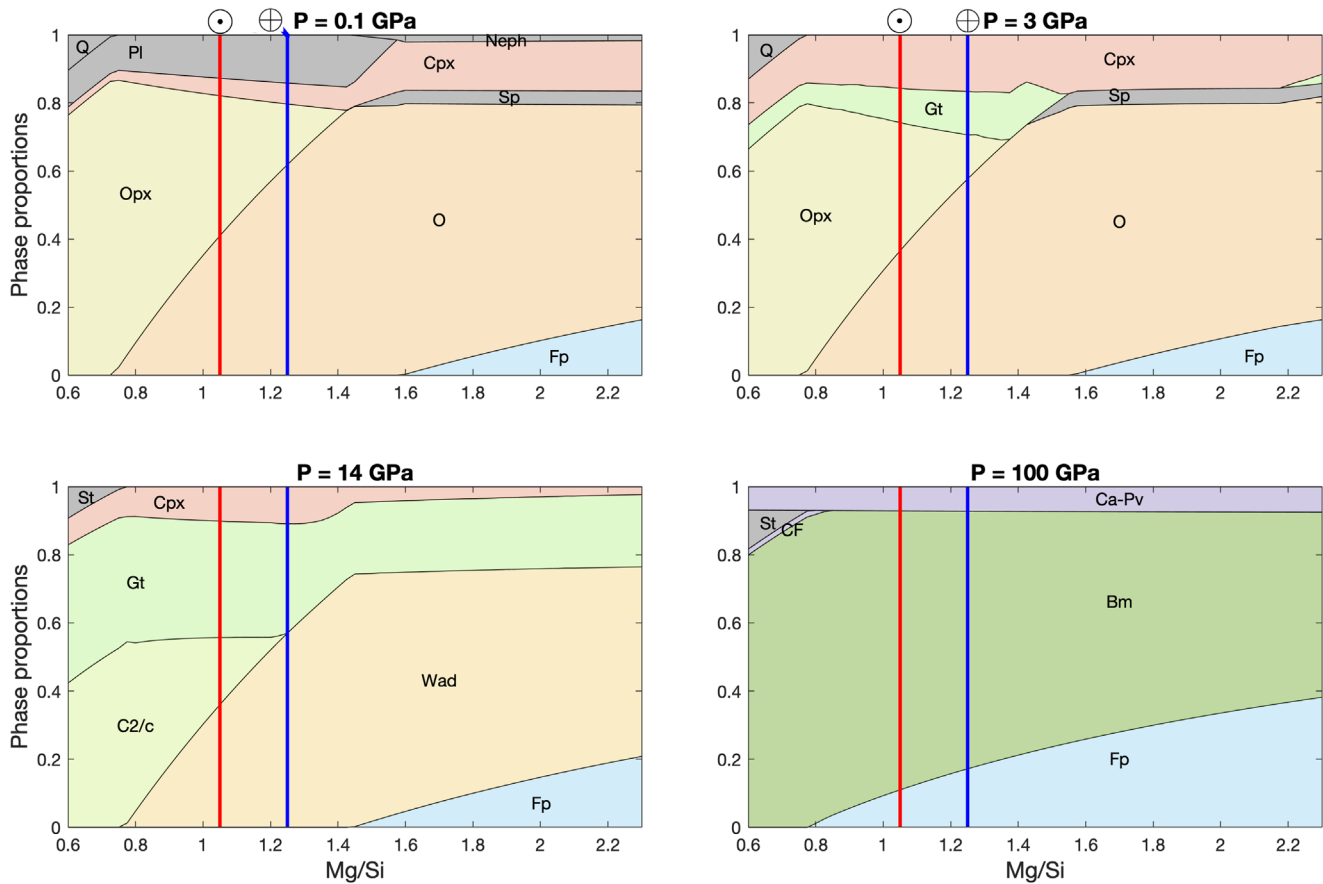
Figure 7. Mantle mineralogy at a range of pressures for planets with an Earth-like composition (composition from McDonough 2003) in terms of Al_2O_3, CaO, and Na_2O, and with Mg/Si varying from 0.6 to 2.0. The FeO abundance is increased linearly with decreasing Mg/Si from 4 to 7 mol%. Mineralogical assemblages are calculated with Perple_X (Connolly 2005), using the thermodynamic database from Stixrude & Lithgow-Bertelloni (2022). Solar (red, ⊙; Lodders et al. 2009) and Earth (blue, ⊕; McDonough 2003) compositions are indicated in all panels. Mineral abbreviations are given in Figure 6.

and hence exotic mantle compositions are rare (see Putirka & Rarick 2019). Also, the Sun's and Earth's compositions are close to the population median (Hinkel & Unterborn 2018; Putirka & Rarick 2019). This compositional variety is mirrored in a diversity in mantle mineralogy, and thus planet properties.

The compositional variety of stars we consider here is partly due to local variation in the solar neighborhood, and partly due to a spread in age (i.e., GCE; Burbidge et al. 1957; Frank et al. 2014; Lugaro et al. 2018). In the GCE effect, the average heavy-element content (heavier than H and He) of stars increases with time. Further, the production of iron is more efficient than that of magnesium, thereby increasing galactic Fe/Mg (see Figures A2(a)–(c), and Figure A3; Matteucci & Greggio 1986; Thielemann et al. 2002; Bensby et al. 2014). Also, it is found that stellar Mg/Si tends to decrease with increasing Fe/H, suggesting that Mg/Si will decrease over time (see Figure A2(d); Frank et al. 2014; Adibekyan et al. 2015; Bedell et al. 2018). Thus, newly formed planets tend to have larger cores, as we predict for HIP 38647, and mantles with larger abundances of stronger minerals such as bridgmanite, quartz, and stishovite. Finally, Ca/Al and minor-element fraction only marginally evolve with time (see Figures A2(e), (f), and Figure A3). As stellar heavy elements generally increase with time, it is more useful to compare age effects and planet properties to stellar ratios of heavy elements (e.g., Mg/Si, Fe/Mg, Ca/Al), rather than classical H-normalized

compositions (see, e.g., the age evolution of Fe/H with Fe/Mg; see Figures A2(a), (b)).

In turn, the concentration of heat-producing elements decreases over time (Frank et al. 2014), leading to less heat production in the interiors of newly formed planets. The radiogenic heat budget of a planet can contribute to thermal evolution and the propensity of a planet toward plate tectonics (O'Neill et al. 2007; Stein et al. 2013). Further, Bitsch & Battistini (2020) find that water abundance systematically decreases with increasing metallicity, which itself decreases with age, due to the increasing abundances of C and S. This implies that planets formed around young stars are relatively dry, and should have lower oxygen fugacities than older planets, leading to even larger CMFs. For our selected sampled-based compositions, planets formed around the old star HIP 99651 ("sample low M_c") would accrete in the most water-rich disk, while planets formed around the younger HIP 90055 ("sample high minor") would accrete in the most water-poor disk.

Previous work has shown a difference in composition between stars of the thick and thin disk populations of the Milky Way (Bensby et al. 2014; Santos et al. 2017; Cabral et al. 2019). Our Galaxy can be divided into multiple populations based on movement and age, where the latter links back to composition. For example, we find within our data that thick-disk stars are less metal-rich than thin-disk stars (Figure A4). Planets in the thick-disk population also typically have higher Mg/Si and lower CMFs, as expected from their age (Figures A2(c), (d), and Figure A3). Therefore, the addition
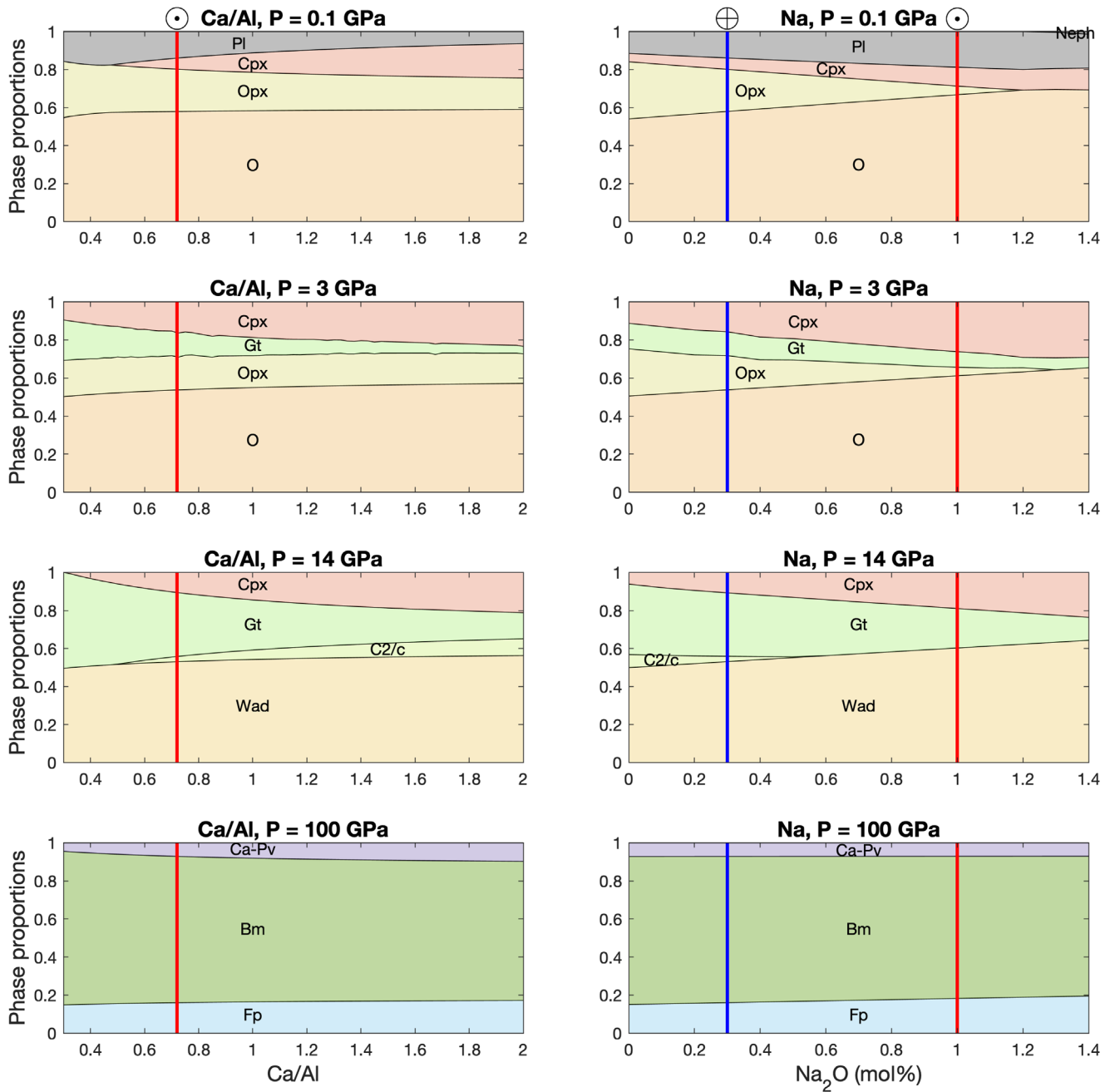
Figure 8. Mantle mineralogy at a range of pressures for planets with an Earth-like composition (composition from McDonough 2003) in terms of FeO, MgO, and SiO$_2$, and with Ca/Al varying from 0.3 to 1.7 (left) and Na$_2$O abundances ranging from 0 to 1 mol% (right). Mineralogical assemblages are calculated with Perple_X (Connolly 2005), using the thermodynamic database from Stixrude & Lithgow-Bertelloni (2022). Solar (red, ⊙; Lodders et al. 2009) and Earth (blue, ⊕; McDonough 2003) compositions are indicated in all panels (solar and Earth Ca/Al coincide). Mineral abbreviations are given in Figure 6.

of the thick-disk population to our sample increases the width of the core-size distribution.

Eight of our sample-based representative planet compositions are based on individual stars (listed in Table 5). These stars do not have any currently detected planets. The stars we chose to exemplify eight of our representative compositions show a spread of metallicity ([Fe/H]), ages, spectral types, distances, and stellar population according to our selection. Therefore, any trend of planet composition with stellar properties should, in principle, be covered by our selection. We find some minor trends between composition and spectral type (see Figure A1), but they are not sufficient to require splitting the population according to their host-star type.

4.2. Devolatilization

The key link between stellar observations and our data set of modeled terrestrial-type exoplanets is element depletion due to devolatilization. The depletion factors we use in this work are calculated according to the elemental abundances in Earth and the Sun, and the 50% condensation temperatures of each element. Comparing various sources for solar abundances (see Asplund et al. 2005, 2009; Lodders et al. 2009), Earth

Table 5
Properties of the Eight Stars We Adopt for the Sample-based Representative Cases

Planet	Star	Spectral Type	Distance (pc)	Age (Gyr)	Mass ($M_\odot$)	[Fe/H]	Population
Earth	Sun	G2V	0	4.5	1	0	Thin
Sample high M_c	HIP 38647	G3V	36	1.35[a]	1.03	0.042	Thin
Sample low Mg/Si	HIP 83069	F8	70	4.7[b]	1.15	−0.16	Thin
Sample high minor	HIP 90055	K2	40	6.47[c]	0.8	0.22	
Sample high Ca/Al	HIP 46639	G0	170	8.38[a]	1.11	−0.04	Thin
Sample low M_c	HIP 99651	K2V	35	5.7[d]	0.89	−0.80	Thin
Sample high Mg/Si	HIP 50493	F6V	36	2.46[b]	1.30	0.04	Thin
Sample high Na	HIP 51028	G0V	107	6.38[b]	1.13	−0.61	Thin
Sample low minor	HIP 113514	G0	54	12.45[e]	1.04	−0.55	Thick

Notes. Distances are from the Hypatia catalog and are, therefore, a literature average. Ages are from various sources. Population refers to the distinction between the thick and thin disk stellar populations in the Milky Way (Santos et al. 2017).
[a] Standford-Moore et al. (2020).
[b] Mints & Hekker (2017).
[c] da Silva et al. (2021).
[d] Tsantaki et al. (2013).
[e] Ramírez et al. (2012).

composition (see McDonough 2003; Wang et al. 2018), and condensation temperature (see Lodders 2003; Wood et al. 2019) shows that the depletion factors we use here (see Table 1) are robust for most elements, and strongly bound by thermodynamical principles (e.g., first ionization potential of the elements). Only the depletion factor for Na varies significantly between sources (i.e., by up to 50%), while simultaneously Na is the element with the largest depletion by devolatilization among the elements we consider here. If we had assumed Na abundances similar to bulk stellar values in Figure 8, the corresponding range would be 0.4–1.4 mol% Na_2O. Decreasing the Na depletion factor would have little effect on lower-mantle mineralogy, but would further stabilize clinopyroxene, and may lead to even lighter and more buoyant crusts (see Earth and Sun in Figure 8).

The devolatilization trend shows that planets are progressively more depleted in elements with lower condensation temperatures, below a certain cut-off temperature (around 1400 K; Wang et al. 2019a). The slope of this depletion trend depends mainly on the width of the feeding zone (see Earth to Vesta; Sossi et al. 2022), while the cut-off temperature depends mainly on the distance to the host star. Applying the Earth–Sun devolatilization trend to exoplanets inherently assumes that the planet is formed in the habitable zone of its host star, and its feeding zone samples material with a similar range of volatile depletion as Earth's. Planet migration and disk dynamics may affect the cut-off temperature and slope of the devolatilization disk. Within the elements we consider, this would mainly affect the depletion of Na, which would be more abundant for planets forming further out. The moderately refractory elements Fe, Mg, and Si could be more depleted in planets forming closer to the star than considered here, leading to an enrichment in Ca and Al.

Depletion factors are based on condensation temperatures for multiple composite minerals, which for most of our elements are similar (Lodders 2003). Hence, moderate compositional variation will not significantly affect the 50% condensation temperatures, except perhaps for extreme stellar compositions (e.g., sulfur for extremely low Fe/S; Jorge et al. 2022), which are, however, beyond the range of our data. How composition will affect planetary devolatilization is still an ongoing

investigation (Wang et al. 2020; Sossi & Wang 2022). For example, the condensation temperature of oxygen varies with stellar composition due to its binary nature as a refractory element (in silicates) and a volatile element (in volatiles such as water). Within our assumption of constant fO_2, our planet oxygen budgets imply that 6.8%–28% of available oxygen (see Figure A5) has condensed as refractory compounds. The corresponding effective condensation temperatures for oxygen range from 721 to 968 K, comparable to the value for Earth from Wang et al. (2019a) of 875 ± 45 K.

Planet formation is complex and chaotic (Morbidelli & Raymond 2016), but the stochastic nature of this process yields a smooth pattern of volatile depletion for planets like Earth, dictated by the central limit theorem, despite various thermal and nonthermal effects (Sossi et al. 2022). This supports that an Earth-like devolatilization trend is a general result of rocky planet formation. For example, Wang et al. (2022b) argue that the devolatilization trends of Venus and Mars may not be significantly different from that of Earth, based on the currently yet-large uncertainties in their individual bulk compositions (e.g., Morgan & Anders 1980; Taylor 2013; Sossi & Fegley 2018; Wang et al. 2018; Yoshizaki & McDonough 2020; Shah et al. 2022). If we arbitrarily increase the uncertainty range of the adopted Sun-to-Earth devolatilization model, as practised in Wang et al. (2022b), it would increase the uncertainties of our compositional estimates for individual planets. However, the results of both our population analysis and their bounds in terms of our representative compositions should remain robust, particularly in terms of major elements, which are almost unaffected by devolatilization (Figure 2(a)).

Our approach excludes a few classes of extreme planet compositions. First, extremely carbon-rich planets have been theorized for stars with molar C/O greater than 0.8 (Bond et al. 2010; Moriarty et al. 2014), suggested to form a thick crust of graphite and diamond (Hakim et al. 2019). We find that only about 5% of the stars in the Hypatia and GALAH catalogs have C/O ratios greater than 0.8, most of which have error bars stretching below 0.8. Second, Ca-Al-rich planets are theorized to form in environments close to the star, where most elements except Ca and Al cannot condense due to the high temperature

(Dorn et al. 2019). These planets are implicitly assumed to form in situ without having accreted mixed material likely transported from the outer to the inner disk. However, due to the low abundances of Ca and Al compared to Fe, Mg, and Si, these planets (if they exist) will mostly be very small. Lastly, water worlds have been predicted, i.e., terrestrial planets with a thick layer of water and ice on the surface (e.g., Kuchner 2003; Unterborn et al. 2018; Acuna et al. 2021; Krissansen-Totton & Fortney 2022). If such a layer of water is sufficiently large, it could fundamentally alter the planetary interior dynamics by suppressing mantle melting and crust formation (Unterborn et al. 2018). However, water delivery to rocky planets is a highly debated topic, and it is currently not possible to link water delivery to stellar observations.

4.3. Core–Mantle Differentiation

We find CMFs ranging from 18 to 35 wt% (Figure 3), indicating that Earth (32.3 wt%) has a relatively large core compared to the modeled exoplanet population. We underestimate the Earth's CMF based on solar abundances by 1.5 wt% (Figure 3). The Earth has elevated Fe/Mg compared to the Sun, which could be attributed to secondary fractionation processes (O'Neill & Palme 2008), or it can be treated as a statistical residual to the devolatilization trend (see Wang et al. 2022b for more details). Overall, we underestimate exoplanet CMF by about 1.5 wt%, which is within measurement error. Core size correlates well with stellar [Fe/Mg] (Figure 3), better than with [Fe/H] (e.g., Hinkel & Unterborn 2018). Modeled interior structures based on observed terrestrial-type exoplanet masses and radii display a fairly similar range of CMFs (typically 20–41 wt%; Otegi et al. 2020; Plotnykov & Valencia 2020; Adibekyan et al. 2021; Schulze et al. 2021), except for a small population of super-Mercuries, which have significantly higher CMFs, potentially due to secondary processes (e.g., Aguichine et al. 2020; Scora et al. 2020; Adibekyan et al. 2021). A large portion of the planets in our data set have a smaller core than Earth and thus are expected to maintain hotter interiors (Noack et al. 2014), and are more likely to develop plate tectonics (O'Neill et al. 2020). Core size is only marginally affected by the presence of Ni and S, as we find core light-element content varying by only a few per cent (Figure A7(a)). Molar Fe/Ni can be up to 30% lower than on Earth, leading to slightly larger cores with higher Ni content (Figures A7(c), (d)). However, the resulting increase in core size is less than 1%, and there is no correlation between core Ni content and CMF (Figure A7(d)).

In our study, we base the core–mantle differentiation process on the assumption that our modeled planets have oxygen fugacities similar to Earth. Allowing fO$_2$ to vary could potentially result in planets with core sizes up to 45 wt% (all Fe in the core, given our assumed core light-element compositions), or could, in turn, result in coreless exoplanets (Elkins-Tanton & Seager 2008; Wang et al. 2019b). The oxidation state of a terrestrial planet's interior depends mainly on the accretion rate and timing of influx from planetesimals from further out in the planet-forming disk (Monteux et al. 2018), which tend to be more oxidized (Rubie et al. 2015; Monteux et al. 2018; Cartier & Wood 2019). Oxygen fugacity should vary only moderately (even though to an unknown extent) between planets that orbit their host star in the habitable zone and with masses similar to Earth, as we assume here. Nevertheless, we consider representative compositions with

different fO$_2$, and explore the effect of varying fO$_2$ on the distribution of Fe between the mantle and core (Figure A6).

4.4. Compositional Effects

Based on the inferred variation of terrestrial-type exoplanet compositions, we identify 21 representative planet compositions (3). These representative compositions result in mantle mineral profiles that are usually very similar to, or even the same as, Earth's. However, the relative abundances of inferred mineral species vary significantly between planets, potentially influencing interior properties and, thus, long-term evolution. Thermal evolution of the interior is controlled by convective transport of heat from the core–mantle boundary to the surface. The convective vigor of the mantle material increases with increasing thermal Rayleigh number (e.g., Schubert et al. 2001), which is given by

$$\mathrm{Ra} = \frac{g\rho\alpha\Delta T d^3}{\kappa\eta}, \quad (1)$$

for gravitational acceleration g (m s^{-2}), density ρ (kg m^{-3}), thermal expansivity α (K^{-1}), temperature contrast across the mantle ΔT (K), mantle thickness d (m), thermal diffusivity κ (m^2 s^{-1}), and viscosity η (Pa s). Of these parameters, the compositional effect on α and β is less significant than on d through core size, and on η through mineralogy.

4.4.1. Mantle Viscosity

Bulk mantle viscosity is regulated by relative abundances of strong and weak mineral phases (i.e., high- and low-viscosity phases). In the lower mantle, bridgmanite is up to three orders of magnitude stronger than ferropericlase (Yamazaki & Karato 2001; Tsujino et al. 2022). While all planets have lower mantles with high bridgmanite abundances, some are almost completely lacking in ferropericlase (Figure 6(c)), while others have significant abundances of the weak mineral ferropericlase (Figure 6(b)). These planets are expected to have a strongly contrasting lower-mantle viscosity profile, as the weaker phase tends to have a more significant effect on viscosity due to formation of interconnected weak layers (Yamazaki & Karato 2001; Thielmann et al. 2020). Further, our representative planets exhibit variable but overall small amounts of Ca-perovskite. The phase Ca-perovskite has typically been considered to be even stronger than bridgmanite and ferropericlase (Miyagi et al. 2009), but recent experimental studies indicate that it may be significantly weaker than both these minerals (Shieh et al. 2004; Immoor et al. 2022). The highest Ca-perovskite abundance of our compositions is 10 vol%, which may be sufficient to form interconnected weak layers (Yamazaki & Karato 2001; Thielmann et al. 2020), thereby decreasing mantle viscosity, if it is indeed weaker than other lower-mantle phases.

Meanwhile, the upper-mantle viscosity is mainly controlled by olivine and pyroxene. In the upper mantle, our representative planet compositions show a huge range from 10% to 80% olivine (Figure 6). While surface observations indicate that pyroxene is stronger than olivine (Tikoff et al. 2010), other studies suggest that the pyroxene/olivine ratio has limited effects on bulk rock viscosity as long as both phases are present (e.g., Tasaka et al. 2013; Hansen & Warren 2015). Some of our representative planets exhibit ferropericlase in the upper mantle, a phase with a viscosity about one order of magnitude

lower than that of olivine or pyroxene (Stretton et al. 2001; Bystricky et al. 2006). Observations of polluted white dwarfs in the solar neighborhood confirm the possibility of an upper mantle containing ferropericlase (Putirka & Xu 2021). While the presence of ferropericlase in exoplanet upper mantles has been derived by previous studies (e.g., Wang et al. 2022b), it is currently not well studied. It is likely to be relevant for planet evolution studies, as it directly affects upper-mantle viscosity, which is an important parameter for determining the propensity of a planet toward plate tectonics (Korenaga 2010; Van Heck & Tackley 2011).

The polluted white dwarf observations also indicate the presence of planets with quartz in the upper mantle. Putirka & Rarick (2019) find a tiny population of planets where pure SiO_2 could potentially be present in their mantles (although they do not employ a Gibbs energy minimization algorithm). While these compositions fall outside our range of representative compositions, they are permitted considering measurement errors (Figure 7). Further, assuming that the core does not contain Si decreases the mantle Mg/Si of our lowest-Mg/Si composition such that a few vol% of quartz, coesite, and stishovite are stabilized. We expect the abundance of SiO_2 phases in these planets to be small, however (see Figure 7), and only to have a minor impact on planetary evolution.

We predict the mantle mineralogy of planets with our representative compositions (Table 3), using the Gibbs energy minimization algorithm Perple_X (Connolly 2005). To accurately determine planet mantle mineralogy, the stellar composition should be known to a precision of $\lesssim 0.025$ dex (Wang et al. 2022b), which is significantly smaller than available uncertainties in the Hypatia and GALAH catalogs, and the vast majority of our planets cannot be constrained to this level of accuracy. That is why we approach this task by considering the entire population; while individual planet compositions should be regarded with appropriate caution, the overall trends we find here are robust. Further, our 21 sets of representative planets are meant to illustrate the limits of the population in terms of composition, which will not change significantly even when individual planet compositions shift within the current abundance uncertainties.

4.4.2. Other Compositional Effects

The melting behavior of planetary mantles is influenced by both the mineral species in the upper mantle (where the vast majority of melting occurs) and the iron content of those minerals. Olivine melts at higher temperatures than pyroxene and garnet, and Fe-rich olivines and pyroxenes melt at lower temperatures than their Fe-poor equivalents (Hirschmann 2000; Kiefer et al. 2015). Planet mantles with higher Ca/Al have also been found to melt at lower temperatures than their low-Ca/Al counterparts, even when the mineralogy is otherwise very similar (Brugman et al. 2021). Therefore, we expect some variation in the degree of melting and volcanism among our planets, which will in turn affect mantle outgassing and atmosphere–interior interaction (e.g., Noack et al. 2017; Dorn et al. 2018; Spaargaren et al. 2020; Gaillard et al. 2021). Further, due to the thermostat effects caused by the temperature dependence of viscosity (Tozer 1965) and, for hot planets, by magmatism (Ogawa & Yanagisawa 2011), the mantle geotherm is expected to evolve close to the solidus of the upper mantle. Thus, the upper-mantle mineralogy strongly affects planetary thermal evolution.

Aside from viscosity, mineralogy also affects mantle dynamics in different ways. On Earth, the ringwoodite-bridgmanite+ferropericlase phase transition at 660 km depth creates a boundary between the upper and lower mantle that impedes convection (Schubert et al. 1975; Christensen & Yuen 1985). Some of our planets are richer in ringwoodite than Earth, which could perhaps lead to doubled-layered convection instead of whole-mantle convection. This is most likely to happen where the olivine fraction is highest, around Mg/Si = 1.5. In contrast, some of our planets have very little ringwoodite, potentially promoting efficient material exchange between the upper and lower mantle (i.e., whole-mantle convection). Further, the water storage capacity in the mantle is expected to vary strongly between exoplanets. Minerals with high water storage capacity, such as wadsleyite and ringwoodite (e.g., Kohlstedt et al. 1996), are rare in low-Mg/Si planets, which would then be expected to have most of their water budget partitioned to the surface. This difference will impact mantle dynamics (Hirth & Kohlstedt 1996; Korenaga 2011), melting (Katz et al. 2003), and volatile outgassing (Wang et al. 2022a). As both Na and Ca tend to stabilize olivine and its high-pressure polymorphs, these elements contribute toward increased water storage capacity in the mantle, and to potential for double-layered convection. Finally, we expect crustal composition to vary as a function of bulk-planet composition. Planets rich in Na and Si will have more buoyant crusts than Earth, which may render subduction and hence plate tectonics less efficient (Cloos 1993; Unterborn et al. 2017).

We described earlier that stellar composition evolves over time, with recently formed stars being richer in Fe and having lower Mg/Si than stars formed long ago (Section 4.1). Most of these age-related effects work toward changing the typical thermal evolution pathway of a terrestrial planet. The Rayleigh number (Equation (1)) decreases when the material becomes more viscous, either due to lower Mg/Si forming stronger minerals or due to a lower water fraction (e.g., Chopra & Paterson 1984). Further, a larger core makes for a smaller mantle, which decreases the Rayleigh number further. Finally, a higher radiogenic element budget increases internal heating, which in turn increases convective vigor. These factors affect the propensity toward plate tectonics, but are often associated with conflicting results (likelihood as a function of Rayleigh number; cf. Korenaga 2010; Van Heck & Tackley 2011). How these effects compare, and what the effect of the time of formation has on the thermal evolution of a planet and its propensity toward plate tectonics, requires investigation with geodynamical models and will be the subject of future research.

5. Conclusions

We present the plausible range of bulk terrestrial exoplanet compositions in the solar neighborhood by considering terrestrial planets as devolatilized stars compositionally. This approach is based on the assumption that planets form from materials condensed from a nebula that shares the chemical composition of the host star. Further, assuming (to the first order) that devolatilization is a universal process in forming rocky planets, we applied the Earth–Sun depletion factors to a large set of stellar abundances in the solar neighborhood (within 200 pc) and obtain a plausible range as presented.

We find that the compositions of the Sun and Earth are close to the medians of the bulk compositions of the population of

Sun-like stars and the postulated terrestrial-type exoplanets around them. For example, rocky exoplanets span a wide range of relative abundances of Mg and Si, with the Earth and Sun close to averages. Further, exotic compositions (i.e., compositions deviating significantly from Earth's) are rather rare, with most planets having mantles of 90–95 molar% MgO+FeO+SiO$_2$. Core sizes range from 18 to 35 wt%, and show a strong correlation with stellar [Fe/Mg].

Stellar Mg/Si is a valuable indicator for mantle mineralogy. To first order, it can be used to predict lower-mantle mineralogy, specifically the ratio of the strong mineral bridgmanite to the weak mineral ferropericlase, and thus lower-mantle viscosity. In the upper mantle it can indicate the presence of ferropericlase, which has yet to be well studied. The mantle Mg/Si can indicate a transition from ferropericlase-bearing upper mantles (mantle Mg/Si $\geqslant$ 1.6), to strong, quartz-bearing (mantle Mg/Si $\leqslant$ 0.8). Further, both Fe/Mg, which indicates core size, and Mg/Si are correlated with age. Recently formed planets tend to have large cores and stiff mantles, while planets formed long ago tend to have small cores and weak mantles. Additionally, stellar Mg/Si and Na/Mg can be used as indicators for crustal bouyancy, as the crusts of Na- and Si-rich planets tend to have lower density than the crusts of Na- and Si-poor planets. Finally, stars rich in Ca and Fe lead to planet mantles with lower melting temperatures, and can therefore lead to increased volcanism. Thus, the stellar composition, upon a necessary correction of devolatilization, gives a more accurate and complete picture of a planet's properties. Importantly, omitting the correction on stellar abundances would reveal a different nature toward the crustal buoyancy. These properties all contribute toward a planet's tendency toward a mobile-lid regime or a stagnant-lid regime, but much research remains to be done before we can couple stellar composition to this tendency.

Rocky planet composition affects planetary evolution in multiple ways, and it is therefore a crucial component in understanding how rocky planets work. We have taken a first step toward studying this component by placing constraints on the range of potential bulk compositions of terrestrial-type exoplanets. By considering 21 representative compositions that span the full compositional range, we also deliver a convenient reference data set for further numerical, experimental, and observational studies on the effects of rocky exoplanet compositions in the broad context of exoplanet characterization.

Appendix

A.1. Data Conversion and Error Propagation

Stellar abundance data in the Hypatia catalog are available in dex units, [X/H] for element X, while data in the GALAH catalog are available as [X/Fe], alongside [Fe/H]. To convert these to bulk-planet molar composition for the relevant elements (O, Na, Al, Mg, Si, S, Ca, Fe, and Ni), we adopt an approach similar to Hinkel et al. (2022), with the addition of applying depletion factors from Table 1, which we label d_i, where $i = 1,...,9$ corresponds to the nine elements we consider here. We first retrieve bulk-planet abundances X_i before normalizing to bulk-planet concentration in molar parts per million (ppm), C_i. Similar to Equation (14) of Hinkel et al. (2022), and using solar abundances $X_\odot$ from Lodders et al. (2009), we find bulk-planet abundances

$$X_i = 10^{[X_i/H]+X_{\odot,i}+d_i},$$

for the Hypatia data and for GALAH Fe abundances, while for the other GALAH abundances, given in [X/Fe], we use

$$X_i = 10^{[X_i/Fe]+[Fe/H]+X_{\odot,i}+d_i}.$$

Finally, we sum up the abundances of all nine elements we consider here, and normalize to retrieve the bulk-planet composition in molar ppm, $C_i = 10^6 * X_i/\sum_{i=1}^{9} X_i$.

Regarding error propagation, we adopt an approach similar to Equations (19) and (20) from Hinkel et al. (2022), which we adapt for an increased amount of variables. Following Taylor (1997), we know that error propagation of a function $f(x, y)$ follows $\sigma_f = \sqrt{\left(\frac{\partial f}{\partial x}\right)^2 \sigma_x^2 + \left(\frac{\partial f}{\partial y}\right)^2 \sigma_y^2}$. Therefore, for abundances from the Hypatia catalog and Fe abundances from the GALAH catalog, we have

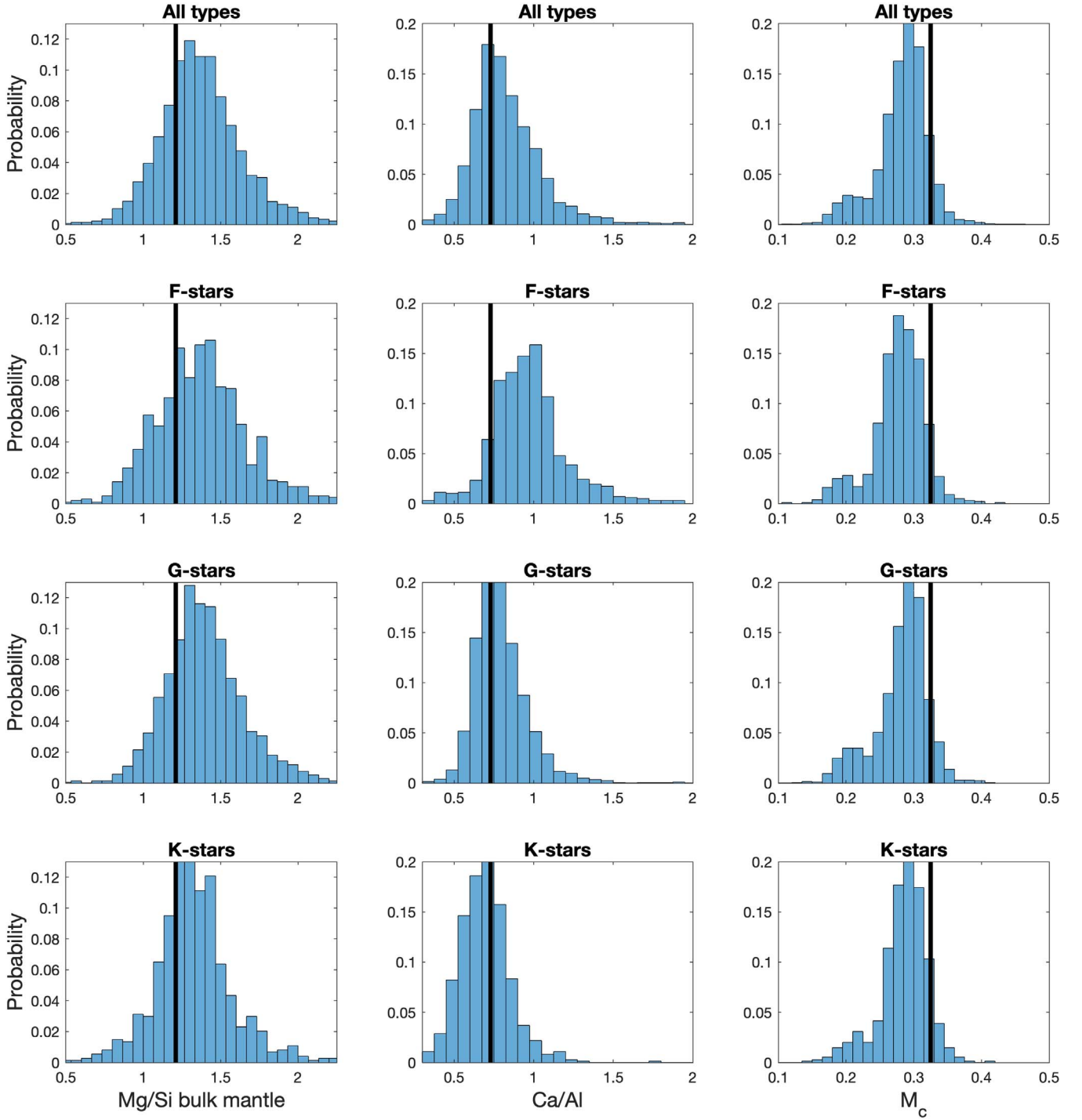$$\sigma_{X_i} = \ln(10)\sqrt{\sigma_{[X_i/H]}^2 + \sigma_{d_i}^2},$$

Figure A1. Modeled planet compositions as a function of spectral class. Comparison of mantle molar Mg/Si (left), mantle molar Ca/Al (middle), and core sizes (right) of our population for all stars and stellar spectral types F, G, and K (top to bottom). Bulk-Earth composition is plotted as a solid black line for comparison (McDonough 2003).

where $\sigma_{[X_i/H]}$ is given by the respective catalog, and σ_{d_i} is given by Table 1. Typical stellar errors are between 0.02 and 0.10 dex. For other elements in the GALAH catalog, we have

$$\sigma_{X_i} = \ln(10)\sqrt{\sigma_{[X_i/Fe]}^2 + \sigma_{[Fe/H]}^2 + \sigma_{d_i}^2},$$

where values of $\sigma_{[X_i/Fe]}$ are given by the catalog. Finally, for converting σ_{X_i} to σ_{C_i}, we need to apply error propagation again, giving us

$$\sigma_{C_i} = \frac{C_i}{\sum_{j=1}^{9} X_j} \sqrt{\left(\sum_{j \neq i} X_j/X_i\right)^2 \sigma_{X_i}^2 + \sum_{j \neq i} \sigma_{X_j}^2}.$$
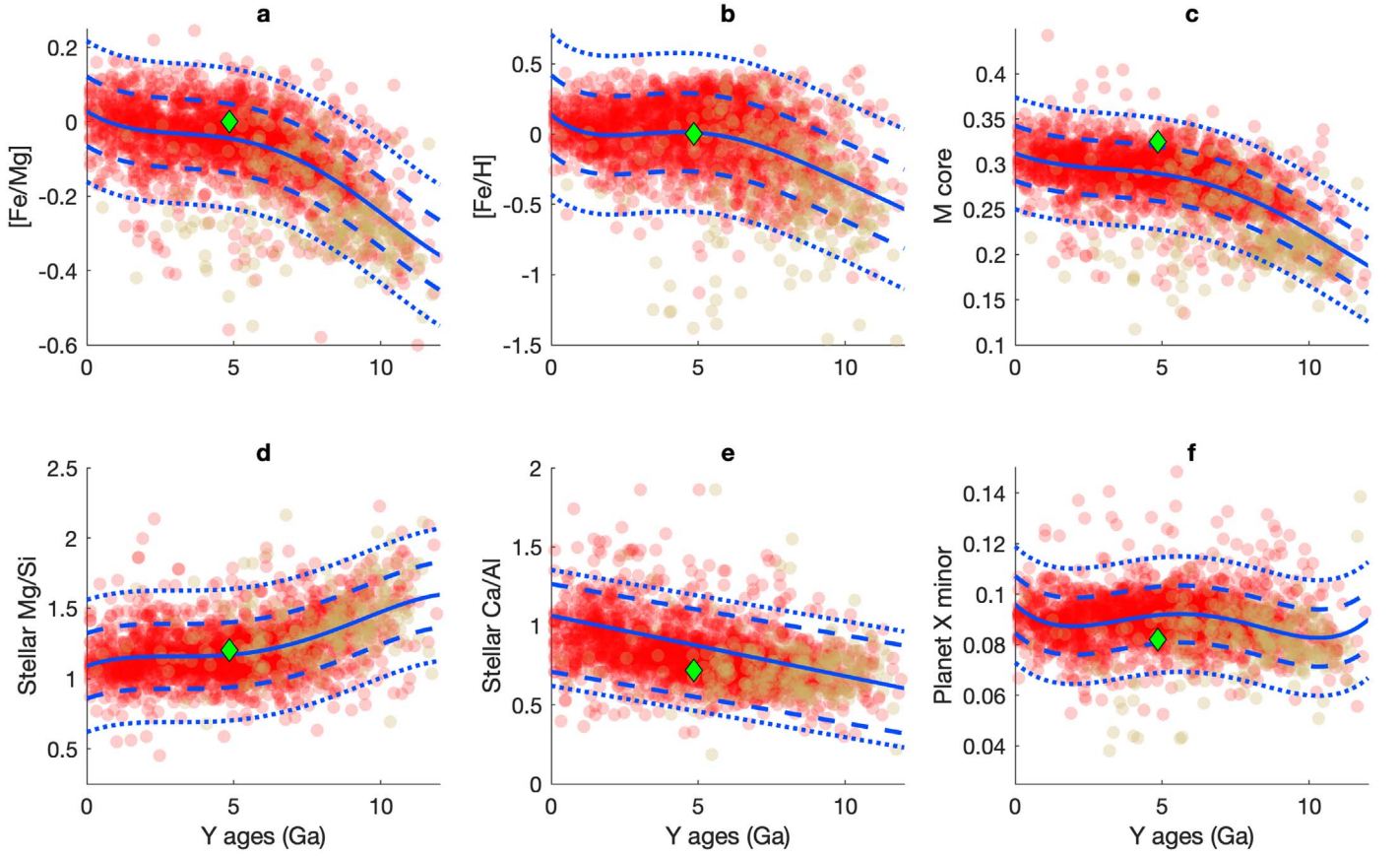
Figure A2. Stellar [Fe/Mg] (a), stellar [Fe/H] (b), core mass fraction (c), stellar molar Mg/Si (d), stellar Ca/Al (e), and planet mantle minor-element fraction (f) as a function of stellar age (in billions of years, Ga), estimated as a function of Y/Mg and Y/Al, based on Equations (6) and (7) from Spina et al. (2018). Stellar compositions are from Hinkel et al. (2014), color-coded for the thin-disk (red) and thick-disk (gold) populations of the Milky Way.

A.2. Age Trend Estimates

We fit polynomials to the age–composition trends shown in Figure A2. The order of the polynomial is decided based on when the rms of the fit stops increasing significantly when adding terms, while the *p*-values of each term are below 0.05. These fits do not change significantly when only considering thin-disk stars. The six polynomials are given as a function of stellar age, *a*, based on the average of the Y/Mg and Y/Al ages from Equations (6) and (7) from Spina et al. (2018):

$$M_{\text{core}} = 0.3122 \pm 0.0069 - 0.0124 \pm 0.00624a$$
$$+ 3.53 \pm 1.75a^2 \cdot 10^{-3}$$
$$- 4.89 \pm 1.85 \cdot 10^{-4}a^3 + 1.72 \pm 0.65 \cdot 10^{-5}a^4, \quad \text{(A1)}$$

$$[\text{Fe/H}] = 0.140 \pm 0.077 - 0.185 \pm 0.066a$$
$$+ 0.079 \pm 0.040a^2 - 0.0135 \pm 0.0069a^3$$
$$+ 9.34 \pm 5.20 \cdot 10^{-4}a^4 - 2.33 \pm 1.39 \cdot 10^{-5}a^5, \quad \text{(A2)}$$

$$[\text{Fe/Mg}] = -0.062 \pm 0.021 - 0.049 \pm 0.019a$$
$$+ 0.0152 \pm 0.0054a^2 - 2.07 \pm 0.57 \cdot 10^{-3}a^3$$
$$+ 7.68 \pm 1.99 \cdot 10^{-5}a^4, \quad \text{(A3)}$$

$$\text{Mg/Si} = 1.089 \pm 0.052 + 0.073 \pm 0.047a$$
$$- 0.027 \pm 0.013a^2 + 3.97 \pm 1.41 \cdot 10^{-3}a^3 - 1.6 \pm 0.5 \cdot 10^{-4}a^4, \quad \text{(A4)}$$

$$\text{Ca/Al} = 0.987 \pm 0.018 - 0.0325 \pm 0.0032a, \quad \text{(A5)}$$

$$X_{\text{minor}} = 0.0959 \pm 0.0025 - 0.0105 \pm 0.0023a$$
$$+ 4.10 \pm 0.65 \cdot 10^{-3}a^2 - 5.47 \pm 0.67 \cdot 10^{-4}a^3$$
$$+ 2.29 \pm 0.24 \cdot 10^{-5}a^4. \quad \text{(A6)}$$

A.3. Compositional Trends

As presented in the main text, we investigated trends in stellar and planetary composition with stellar type, age, and population. The Hypatia and GALAH catalogs contains stars of the F, G, and K-spectral types, which follow slightly different evolutionary pathways. We find some minor trends, where the Ca/Al-distribution of F-type stars skews toward higher values, while K-type stars skew toward lower values (Figure A1). Further, the distribution of mantle Mg/Si and core mass seems narrower for K-type stars. These trends are not sufficient to split the population along spectral types in our research. We further looked into trends of composition with age, as described in Section 4.1, and do find meaningful trends here (Figures A2 and A3). This is reflected in the trend of metallicity with Galactic population, as thick disc stars tend to be older and therefore have lower metallicity (Figure A4).

Given our assumptions on bulk planet oxygen fugacity (See Section 2.3), the fraction of oxygen condensed in refractory
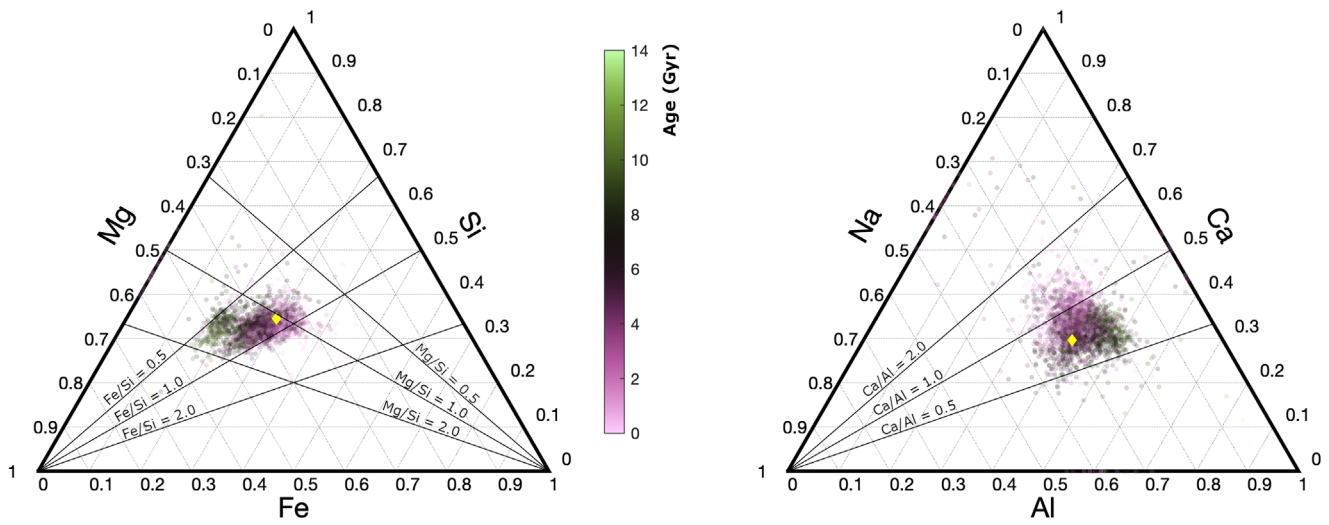
Figure A3. Stellar abundances as contained by the Hypatia catalog (Hinkel et al. 2014), color-coded for stellar age as estimated from stellar Y/Mg and Y/Al (see Equations (6) and (7) from Spina et al. 2018). Solar composition from Lodders et al. (2009) is plotted for reference.
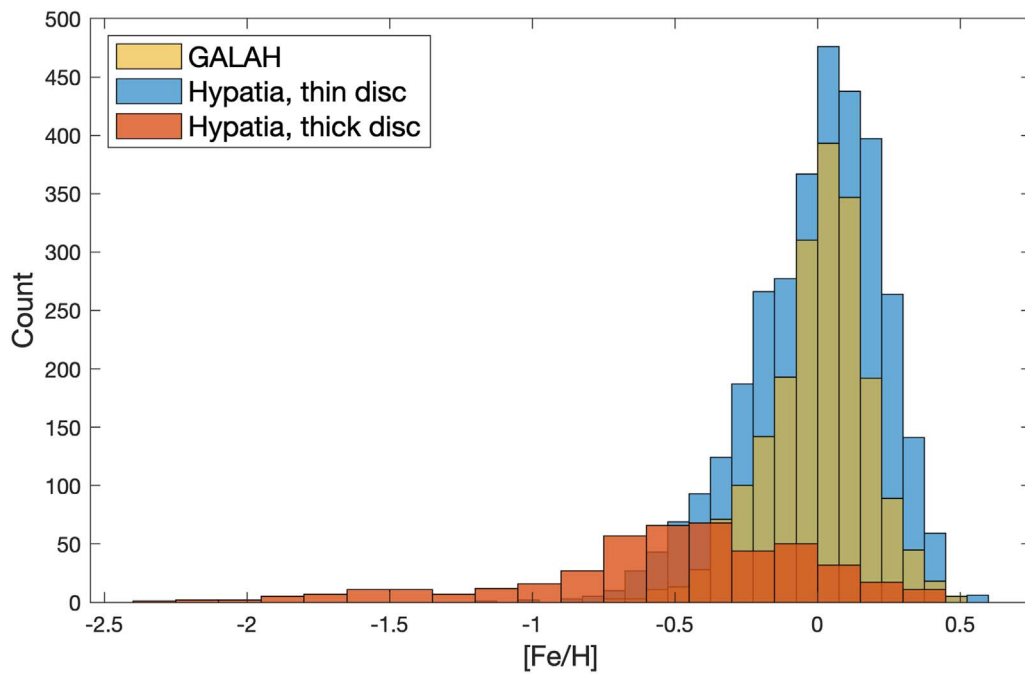

Figure A4. Distribution of stellar metallicity (in terms of [Fe/H] in dex) of our sample. We distinguish between data from the GALAH catalog (green) and the Hypatia catalog for stars from the Galactic thick (brown) and thin (blue) disks.
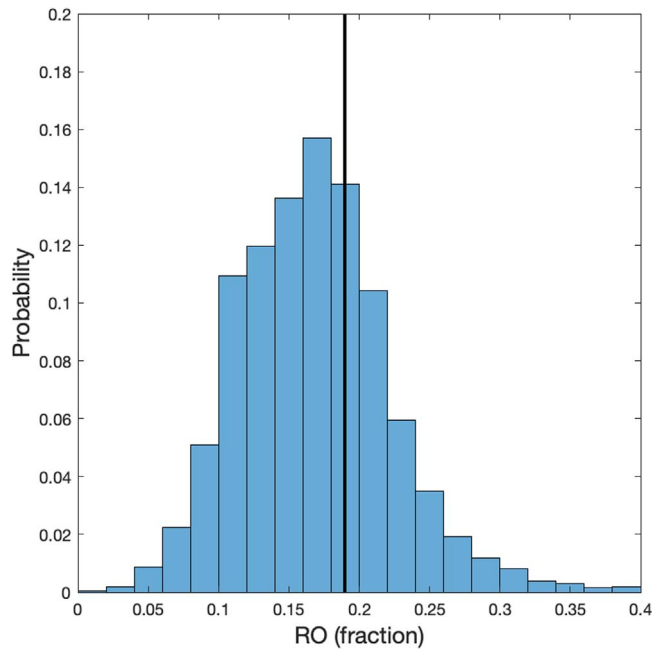
Figure A5. Histogram of refractory oxygen (RO) fractions in our population under the assumption of constant fO_2. This is the fraction of available oxygen that condensed as refractory compounds during planet formation, and is equivalent to the depletion factor for oxygen (see Table 1). The Earth–Sun RO fraction is plotted for comparison (Wang et al. 2019a).
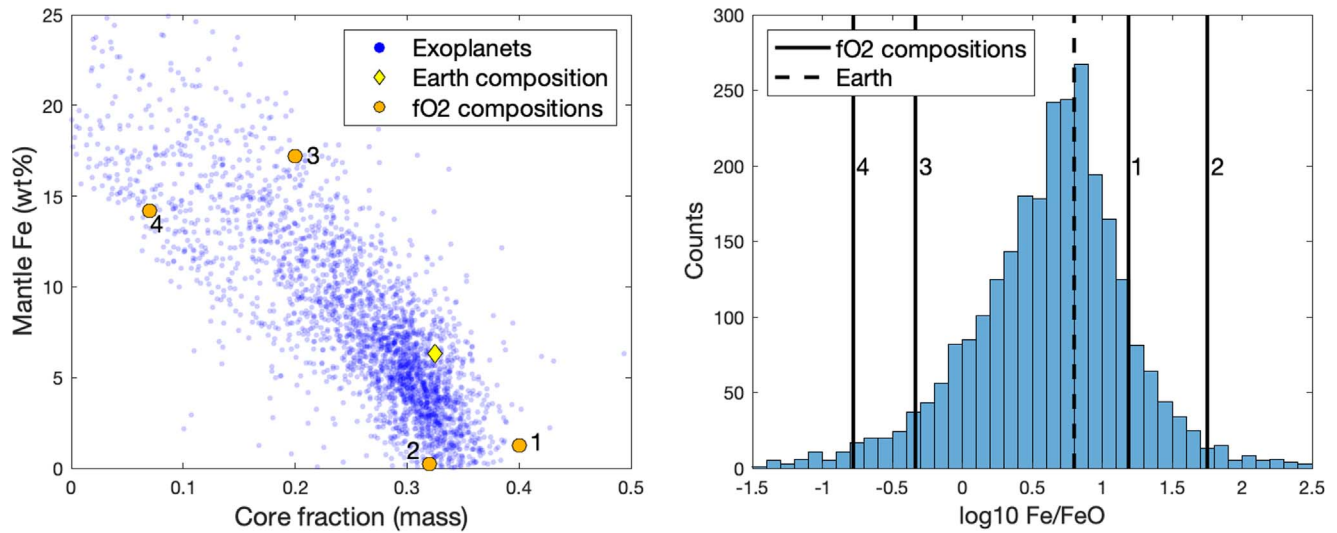
Figure A6. Scatterplot of core mass fraction and mantle iron content (left), and histogram of corresponding bulk-planet Fe/FeO ratio (right), without the assumption of constant fO_2 for all planets (see Section 3.3). Bulk oxygen fugacity is based on stellar composition after devolatilization, after adding a correction for removing coreless planets and extremely reduced planets. Representative compositions synthetic-fO_2 1–4 from Table 3 are plotted in both figures.
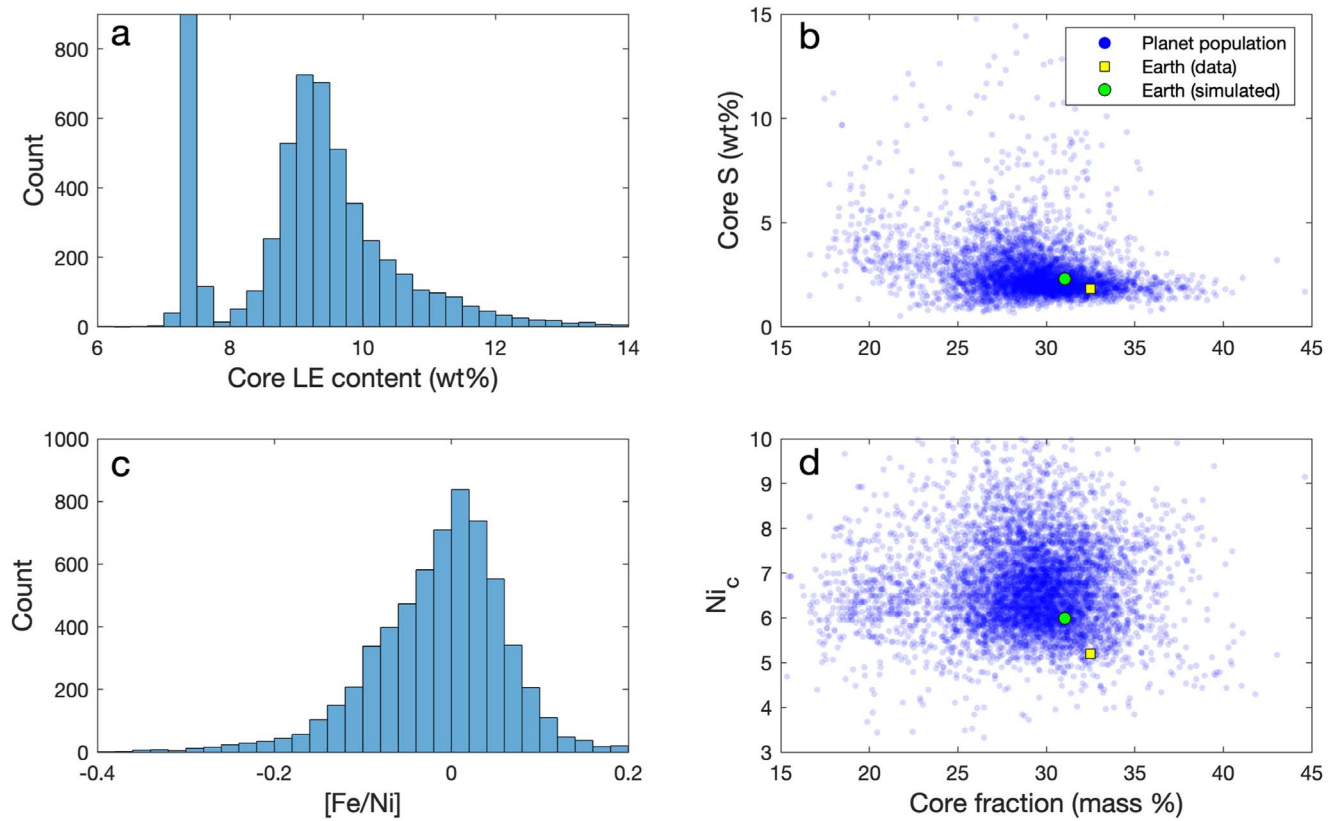
Figure A7. Composition of the cores of exoplanets, compared to Earth from McDonough (2003), and a simulated Earth based on the solar composition Lodders et al. (2009). We plot core light-element content in wt%, which consists of oxygen, silicon, and sulfur (a). The large peak at 7.5 wt% is caused by planet compositions based on stellar compositions from the GALAH catalog, which does not contain S abundances. Further, core S concentration in wt% is plotted against bulk-planet Fe+Ni content (b). We plot the distribution of stellar [Fe/Ni] (c). Finally, we plot core molar Ni content against bulk core mass fraction (d).
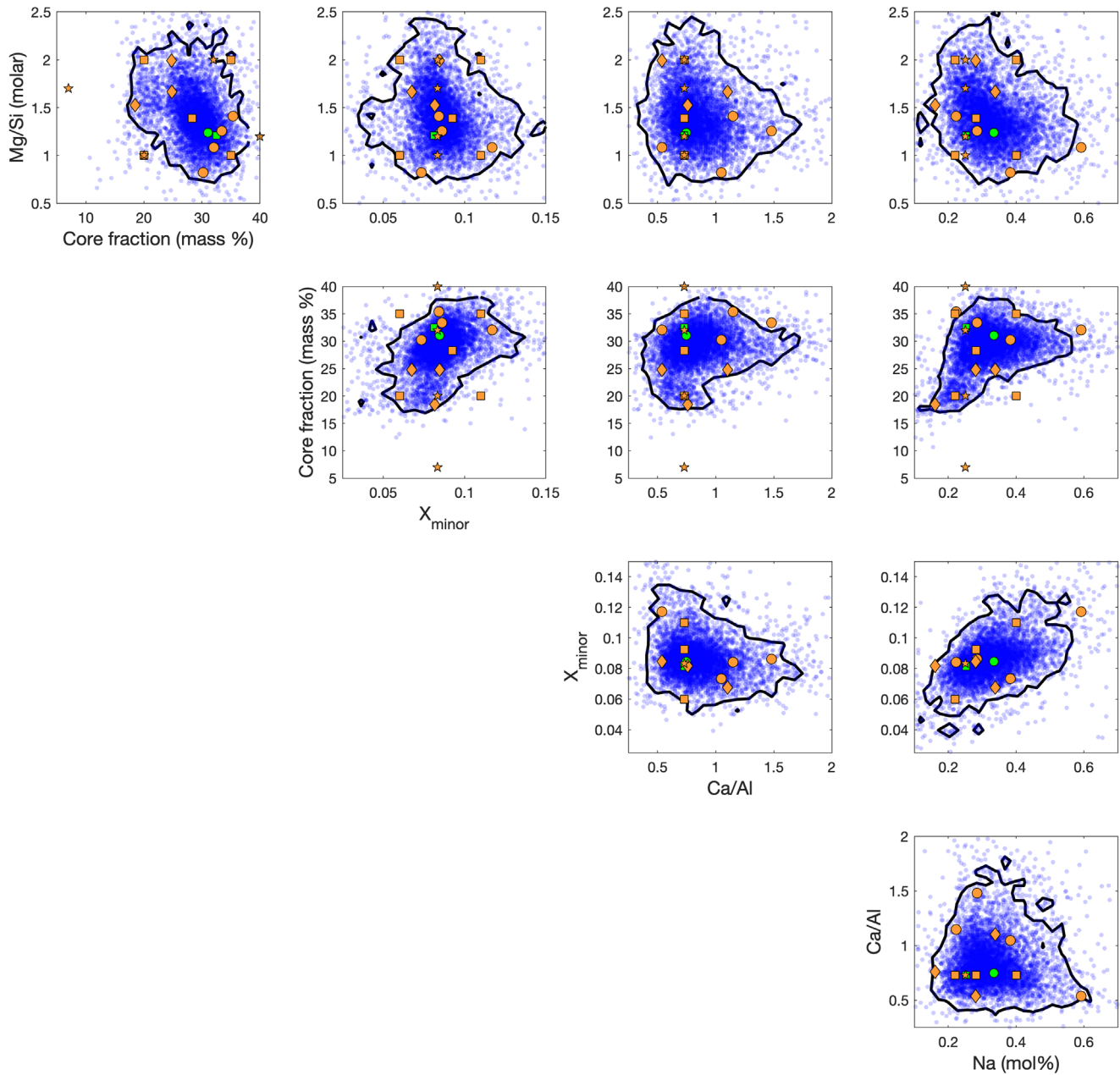
Figure A8. Scatter plots of bulk terrestrial exoplanet compositions for all compositional quantities, showing compositional trends. The contours contain 95% of the compositions. Orange dots and diamonds show the high-Fe/Mg and low-Fe/Mg sample-based compositions, orange squares show the eight synthetic compositions, respectively, and the stars show the four synthetic-fO$_2$ compositions. The green square represents the Earth's composition (McDonough 2003), while the green circle represents the composition of a simulated planet based on a star with a protosolar composition (Wang et al. 2019a).
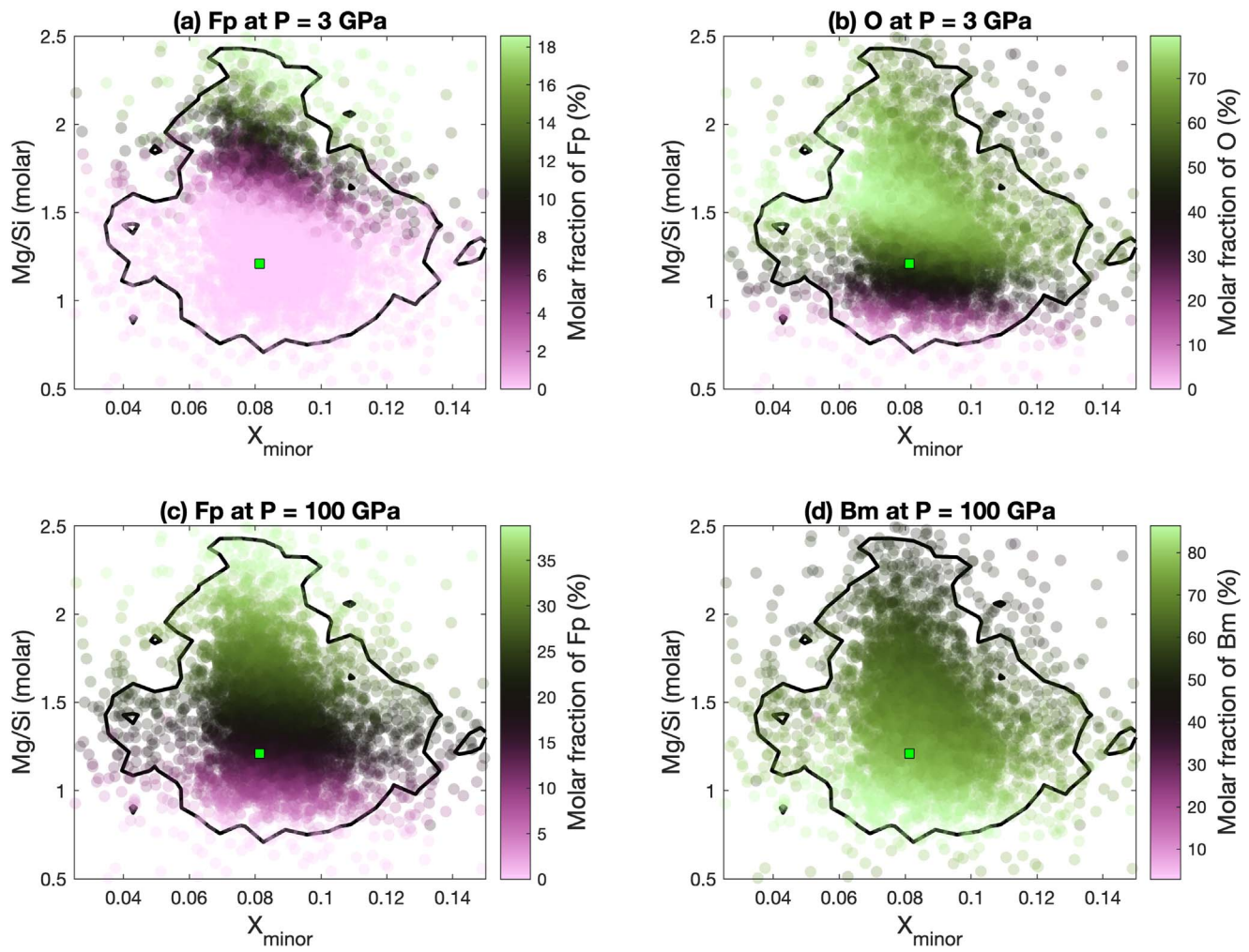
Figure A9. Molar fractions of ferropericlase ((a) and (c)), olivine (b), and bridgmanite (d), at 3 (top) and 100 (bottom) GPa. Mineralogical assemblages are calculated from mantle compositions based on stellar abundances for all 6207 data points in our population, using Perple_X (Connolly 2005) with the thermodynamic database from Stixrude & Lithgow-Bertelloni (2022). The Earth's composition (yellow square) is from McDonough (2003).
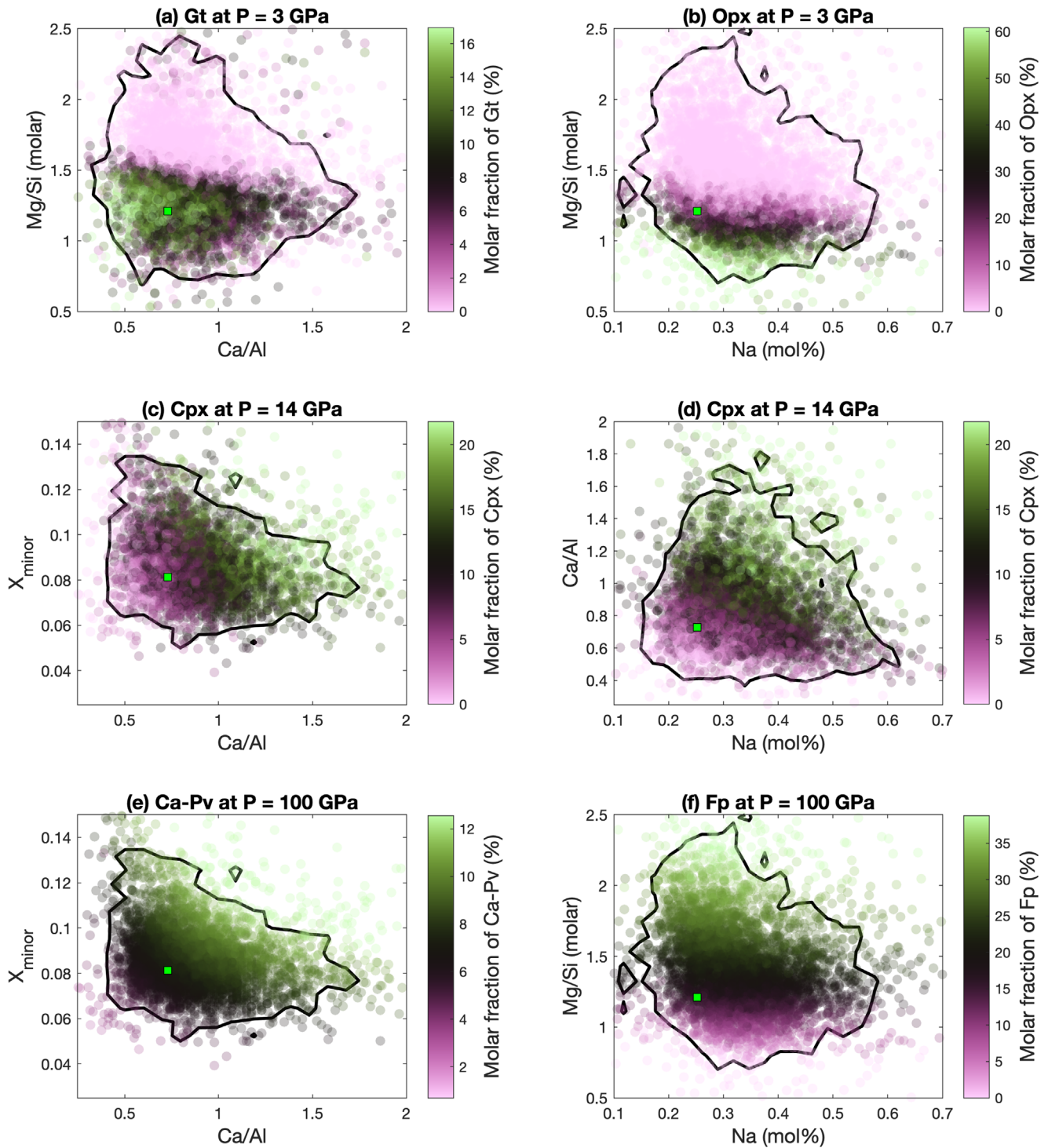
Figure A10. Molar fractions of garnet (a), orthopyroxene (b), clinopyroxene ((c) and (d)), Ca-perovskite (e), and ferropericlase (f), at 3 (top), 14 (middle), and 100 (bottom) GPa. Mineralogical assemblages are calculated from mantle compositions based on stellar abundances for all 6207 data points in our population, using Perple_X (Connolly 2005) with the thermodynamic database from Stixrude & Lithgow-Bertelloni (2022). The Earth's composition (yellow square) is from McDonough (2003).

compounds (i.e., silicates) depends on stellar composition, and deviates from Solar Values (Figure A5). We do include some cases where we adjust planet oxygen fugacity for stellar oxygen abundance, to investigate our oxygen fugacity assumption (Figure A6). Further, our core sizes and composition depends on stellar abundances, specifically on the Fe/Ni ratio and stellar S abundances (Figure A7).

After determining mantle compositions, we select representative compositions (see Table 3) to investigate in more detail based on various trends as shown in Figure A8. Mantle mineralogy is studied to greater detail for these compositions (see, e.g., Figure 6), but for illustration, we include trends of some important minerals with composition (Figures A9 and A10) as a complement to Figures 7 and 8.

ORCID iDs

Rob J. Spaargaren ⬮ https://orcid.org/0000-0002-4080-7269
Haiyang S. Wang ⬮ https://orcid.org/0000-0001-8618-3343
Stephen J. Mojzsis ⬮ https://orcid.org/0000-0003-0000-125X
Maxim D. Ballmer ⬮ https://orcid.org/0000-0001-8886-5030
Paul J. Tackley ⬮ https://orcid.org/0000-0003-4878-621X

References

Acuna, L., Deleuil, M., Mousis, O., et al. 2021, A&A, 647, A53
Adibekyan, V., Dorn, C., Sousa, S. G., et al. 2021, Sci, 374, 330
Adibekyan, V., Santos, N. C., Figueira, P., et al. 2015, A&A, 581, L2
Aguichine, A., Mousis, O., Devouard, B., & Ronnet, T. 2020, AJ, 901, 97
Alibés, A., Labay, J., & Canal, R. 2001, AnA, 370, 1103
Anders, E., & Grevesse, N. 1989, GeCoA, 53, 197
Asplund, M., Grevesse, N., & Sauval, A. J. 2005, in ASP Conf. Ser. 336,
    Cosmic Abundances as Records of Stellar Evolution and Nucleosynthesis,
    ed. T. G. Barnes, III & F. N. Bash (San Francisco, CA: ASP), 25
Asplund, M., Grevesse, N., Sauval, A. J., & Scott, P. 2009, ARA&A, 47, 481
Bedell, M., Bean, J. L., Meléndez, J., et al. 2018, ApJ, 865, 68
Bensby, T., Alves-Brito, A., Oey, M., Yong, D., & Melendez, J. 2011, ApJ,
    735, L46
Bensby, T., Feltzing, S., Lundström, I., & Ilyin, I. 2005, A&A, 433, 185
Bensby, T., Feltzing, S., & Oey, M. 2014, A&A, 562, A71
Bitsch, B., & Battistini, C. 2020, A&A, 633, A10
Bland, P. A., Alard, O., Benedix, G. K., et al. 2005, PNAS, 102, 13755
Bond, J. C., O'Brien, D. P., & Lauretta, D. S. 2010, ApJ, 715, 1050
Bonsor, A., Carter, P. J., Hollands, M., et al. 2020, MNRAS, 492, 2683
Bonsor, A., Jofré, P., Shorttle, O., et al. 2021, MNRAS, 503, 1877
Brown, J., & Shankland, T. 1981, GeoJI, 66, 579
Brugman, K., Phillips, M., & Till, C. 2021, JGRE, 126, e06731
Bryson, S., Kunimoto, M., Kopparapu, R. K., et al. 2020, AJ, 161, 36
Buchhave, L. A., Latham, D. W., Johansen, A., et al. 2012, Natur, 486, 375
Buder, S., Asplund, M., Duong, L., et al. 2018, MNRAS, 478, 4513
Burbidge, E. M., Burbidge, G. R., Fowler, W. A., & Hoyle, F. 1957, RvMP,
    29, 547
Bystricky, M., Heidelbach, F., & Mackwell, S. 2006, Tectp, 427, 115
Cabral, N., Lagarde, N., Reylé, C., Guilbert-Lepoutre, A., & Robin, A. 2019,
    A&A, 622, A49
Carter-Bond, J. C., O'Brien, D. P., & Raymond, S. N. 2012, ApJ, 760, 44
Cartier, C., & Wood, B. J. 2019, Eleme, 15, 39
Chopra, P. N., & Paterson, M. S. 1984, JGR, 89, 7861
Christensen, U. R., & Yuen, D. A. 1985, JGR, 90, 10291
Clark, J. T., Clerté, M., Hinkel, N. R., et al. 2021, MNRAS, 504, 4968
Cloos, M. 1993, GSAB, 105, 715
Connolly, J. A. 2005, E&PSL, 236, 524
Corgne, A., Keshav, S., Wood, B. J., McDonough, W. F., & Fei, Y. 2008,
    GeCoA, 72, 574
da Silva, J. G., Santos, N., Adibekyan, V., et al. 2021, A&A, 646, A77
De Silva, G. M., Freeman, K. C., Bland-Hawthorn, J., et al. 2015, MNRAS,
    449, 2604
Dorn, C., Harrison, J. H., Bonsor, A., & Hands, T. O. 2019, MNRAS, 484, 712
Dorn, C., Hinkel, N. R. N., & Venturini, J. 2017, A&A, 597, A38
Dorn, C., Khan, A., Heng, K., et al. 2015, A&A, 577, A83
Dorn, C., Noack, L., & Rozel, A. B. 2018, A&A, 614, A18
Dotter, A., Conroy, C., Cargile, P., & Asplund, M. 2017, ApJ, 840, 99
Doyle, A. E., Young, E. D., Klein, B., Zuckerman, B., & Schlichting, H. E.
    2019, Sci, 366, 356
Elkins-Tanton, L. T., & Seager, S. 2008, ApJ, 688, 628
Frank, E. A., Meyer, B. S., & Mojzsis, S. J. 2014, Icar, 243, 274
Gaillard, F., Bouhifd, M. A., Füri, E., et al. 2021, SSRv, 217, 22
Guerrero, J., Lowman, J. P., Deschamps, F., & Tackley, P. 2018, JGRE,
    123, 1863
Hakim, K., Spaargaren, R., Grewal, D. S., et al. 2019, AsBio, 19, 867
Halliday, A. N., & Porcelli, D. 2001, E&PSL, 192, 545
Hansen, L. N., & Warren, J. M. 2015, JGRB, 120, 2717
Harrison, J. H., Bonsor, A., Kama, M., et al. 2021, MNRAS, 504, 2853
Hinkel, N. R., Timmes, F. X., Young, P. A., Pagano, M. D., & Turnbull, M. C.
    2014, AJ, 148, 54
Hinkel, N. R., & Unterborn, C. T. 2018, ApJ, 853, 83
Hinkel, N. R., Young, P. A., Pagano, M. D., et al. 2016, ApJS, 226, 4
Hinkel, N. R., Young, P. A., & Wheeler, C. H., III 2022, AJ, 164, 256
Hirose, K., Labrosse, S., & Hernlund, J. 2013, AREPS, 41, 657
Hirschmann, M. M. 2000, GGG, 1, 1042

Hirth, G., & Kohlstedt, D. L. 1996, E&PSL, 144, 93
Hollands, M., Gänsicke, B., & Koester, D. 2018, MNRAS, 477, 93
Immoor, J., Miyagi, L., Liermann, H.-P., et al. 2022, Natur, 603, 276
Ishikawa, H. T., Aoki, W., Kotani, T., et al. 2020, PASJ, 72, 102
Javoy, M., Kaminski, E., Guyot, F., et al. 2010, E&PSL, 293, 259
Jorge, D., Kamp, I., Waters, L., Woitke, P., & Spaargaren, R. 2022, A&A,
    660, A85
Katz, R. F., Spiegelman, M., & Langmuir, C. H. 2003, GGG, 4, 1073
Kiefer, W. W. S., Filiberto, J., Sandu, C., & Li, Q. 2015, GeCoA, 162, 247
Kohlstedt, D. L., Keppler, H., & Rubie, D. C. 1996, CoMP, 123, 345
Korenaga, J. 2010, JGRB, 115, B11405
Korenaga, J. 2011, JGRB, 116, B12403
Krissansen-Totton, J., & Fortney, J. J. 2022, ApJ, 933, 115
Kuchner, M. J. 2003, ApJ, 596, L105
Lin, W.-J., Wang, H., Hunt, A., & Quanz, S. 2022, EPSC, 16, 678
Liu, F., Yong, D., Asplund, M., et al. 2020, MNRAS, 495, 3961
Lodders, K. 2003, ApJ, 591, 1220
Lodders, K., Palme, H., & Gail, H.-P. 2009, in Solar System—Landolt-
    Börnstein—Group VI Astronomy and Astrophysics, ed. J. Trümper, Vol.
    4B (Berlin: Springer), 712
Lourenço, D. L., Rozel, A. B., Ballmer, M. D., & Tackley, P. J. 2020, GGG,
    21, e08756
Lugaro, M., Ott, U., & Kereszturi, A. 2018, PrPNP, 102, 1
Matteucci, F., & Greggio, L. 1986, A&A, 154, 279
McDonough, W. F. 2003, in Treatise on Geochemistry 2, ed. H. D. Holland &
    K. K. Turekian, Vol. 3 (3rd edn.; Amsterdam: Elsevier), 559
McDonough, W. F., & Sun, S.-S. S. 1995, ChGeo, 120, 223
Melendez, J., Asplund, M., Gustafsson, B., & Yong, D. 2009, ApJL, 704,
    L66
Mints, A., & Hekker, S. 2017, A&A, 604, A108
Miyagi, L., Merkel, S., Yagi, T., et al. 2009, PEPI, 174, 159
Mojzsis, S. 2022, in Chemical Biology No. 20, Prebiotic Chemistry and Life's
    Origin, ed. M. Fiore (Royal Society of Chemistry), 21
Mojzsis, S. J. 2021, NatAs, 5, 1083
Monteux, J., Golabek, G. J., Rubie, D. C., Tobie, G., & Young, E. D. 2018,
    SSRv, 214, 39
Moore, W. B., & Webb, A. G. 2013, Natur, 501, 501
Morbidelli, A., & Raymond, S. N. 2016, JGRE, 121, 1962
Morgan, J. W., & Anders, E. 1980, PNAS, 77, 6973
Moriarty, J., Madhusudhan, N., & Fischer, D. 2014, ApJ, 787, 81
Mulders, G. D., Pascucci, I., Apai, D., & Ciesla, F. J. 2018, AJ, 156, 24
NASA Exoplanet Science Institute 2022, Planetary Systems, Version: 2022-08-
    16 18:00, NExScI-Caltech/IPAC
Noack, L., & Breuer, D. 2013, Habitability of Other Planets and Satellites
    (Berlin: Springer), 203
Noack, L., & Breuer, D. 2014, P&SS, 98, 41
Noack, L., Godolt, M., Von Paris, P., et al. 2014, P&SS, 98, 14
Noack, L., & Lasbleis, M. 2020, A&A, 638, A129
Noack, L., Rivoldini, A., & Van Hoolst, T. 2017, PEPI, 269, 40
Ogawa, M., & Yanagisawa, T. 2011, JGRE, 116, E08008
O'Neill, C. 2020, P&SS, 192, 105059
O'Neill, C., Lenardic, A., Moresi, L., Torsvik, T. H., & Lee, C.-T. 2007,
    E&PSL, 262, 552
O'Neill, C., Lowman, J., & Wasiliev, J. 2020, Icar, 352, 114025
O'Neill, H. S. C., & Palme, H. 2008, RSPTA, 366, 4205
Otegi, J. F., Bouchy, F., & Helled, R. 2020, A&A, 634, A43
Palme, H., & O'Neill, H. 2013, in Trestise on Geochemistry, ed. A.M. Davis,
    Vol. 2 (2nd edn.; Amsterdam: Elsevier), 1
Parnell, J. 2004, IJAsB, 3, 131
Plotnykov, M., & Valencia, D. 2020, MNRAS, 499, 932
Putirka, K. D., & Rarick, J. C. 2019, AmMin, 104, 817
Putirka, K. D., & Xu, S. 2021, NatCo, 12, 6168
Ramírez, I., Fish, J., Lambert, D. L., & Prieto, C. A. 2012, ApJ, 756, 46
Rubie, D. C., Jacobson, S. A., Morbidelli, A., et al. 2015, Icar, 248, 89
Santos, N. C., Adibekyan, V., Dorn, C., et al. 2017, A&A, 608, A94
Schubert, G., Turcotte, D. L., & Olson, P. 2001, Mantle Convection in the
    Earth and Planets (Cambridge: Cambridge Univ. Press)
Schubert, G., Yuen, D. A., & Turcotte, D. L. 1975, GeoJI, 42, 705
Schulze, J., Wang, J., Johnson, J., et al. 2021, PSJ, 2, 113
Scora, J., Valencia, D., Morbidelli, A., & Jacobson, S. 2020, MNRAS,
    493, 4910
Shah, O., Helled, R., Alibert, Y., & Mezger, K. 2022, ApJ, 926, 217
Shahar, A., Driscoll, P., Weinberger, A., & Cody, G. 2019, Sci, 364, 434
Shahar, A., Ziegler, K., Young, E. D., et al. 2009, E&PSL, 288, 228
Shieh, S. R., Duffy, T. S., & Shen, G. 2004, PEPI, 143, 93
Sossi, P., & Wang, H. 2022, in 16th Euri. Sci. Congr., Vol. 16, EPSC2022–188
Sossi, P. A., & Fegley, B. 2018, RvMG, 84, 393

Sossi, P. A., Klemme, S., O'Neill, H. S. C., Berndt, J., & Moynier, F. 2019, GeCoA, 260, 204

Sossi, P. A., Stotz, I. L., Jacobson, S. A., Morbidelli, A., & O'Neill, H. S. C. 2022, NatAs, 6, 951

Spaargaren, R. J., Ballmer, M. D., Bower, D. J., Dorn, C., & Tackley, P. J. 2020, A&A, 643, A44

Spina, L., Meléndez, J., Karakas, A. I., et al. 2018, MNRAS, 474, 2580

Stamenković, V., Noack, L., Breuer, D., & Spohn, T. 2012, ApJ, 748, 41

Stamenković, V., & Seager, S. 2016, ApJ, 825, 78

Stanford-Moore, S. A., Nielsen, E. L., De Rosa, R. J., Macintosh, B., & Czekala, I. 2020, ApJ, 898, 27

Stein, C., Lowman, J. P., & Hansen, U. 2013, E&PSL, 361, 448

Stixrude, L., & Lithgow-Bertelloni, C. 2022, GeoJI, 228, 1119

Stretton, I., Heidelbach, F., Mackwell, S., & Langenhorst, F. 2001, E&PSL, 194, 229

Takeda, Y. T. 1998, JSG, 20, 1569

Tasaka, M., Hiraga, T., & Zimmerman, M. E. 2013, JGRB, 118, 3991

Taylor, G. J. 2013, ChEG, 73, 401

Taylor, J. 1997, Introduction to Error Analysis, the Study of Uncertainties in Physical Measurements (New York, NY: Univ. Science Books)

Thielemann, F.-K., Argast, D., Brachwitz, F., et al. 2002, The Evolution of Galaxies (Dordrecht: Springer), 25

Thielmann, M., Golabek, G. J., & Marquardt, H. 2020, GGG, 21, e2019GC008688

Tikoff, B., Larson, C. E., Newman, J., & Little, T. 2010, Lsphe, 2, 418

Tozer, D. 1965, RSPTA, 258, 252

Tsantaki, M., Sousa, S., Adibekyan, V. Z., et al. 2013, A&A, 555, A150

Tsujino, N., Yamazaki, D., Nishihara, Y., et al. 2022, SciA, 8, eabm1821

Unterborn, C., & Panero, W. R. 2017, ApJ, 845, 61

Unterborn, C. T., Desch, S. J., Hinkel, N. R., & Lorenzo, A. 2018, NatAs, 2, 297

Unterborn, C. T., Dismukes, E. E., & Panero, W. R. 2016, ApJ, 819, 32

Unterborn, C. T., Hull, S. D., Stixrude, L. P., et al. 2017, LPICo, 2042, 4034

Valencia, D., O'Connell, R. J., & Sasselov, D. 2006, Icar, 181, 545

Valenti, J. A., & Fischer, D. A. 2005, ApJS, 159, 141

Van Heck, H. J., & Tackley, P. J. 2011, E&PSL, 310, 252

Wade, J., & Wood, B. J. 2005, E&PSL, 236, 78

Wang, H., Sossi, P., & Quanz, S. 2020, in 14th Eur. Sci. Congr. Vol. 14, EPSC2020–874

Wang, H. S., Lineweaver, C. H., & Ireland, T. R. 2018, Icar, 299, 460

Wang, H. S., Lineweaver, C. H., & Ireland, T. R. 2019a, Icar, 328, 287

Wang, H. S., Lineweaver, C. H., Quanz, S. P., et al. 2022a, ApJ, 927, 134

Wang, H. S., Liu, F., Ireland, T. R., et al. 2019b, MNRAS, 482, 2222

Wang, H. S., Quanz, S. P., Yong, D., et al. 2022b, MNRAS, 513, 5829

Wänke, H., & Dreibus, G. 1994, RSPTA, 349, 285

Wood, B. J., Smythe, D. J., & Harrison, T. 2019, AmMin, 104, 844

Yamazaki, D., & Karato, S. I. 2001, AmMin, 86, 385

Yoshizaki, T., & McDonough, W. F. 2020, GeCoA, 273, 137

Ziegler, K., Young, E. D., Schauble, E. A., & Wasson, J. T. 2010, E&PSL, 295, 487